NOVA SCHOOL OF SCIENCE & TECHNOLOGY

DEPARTMENT OF PHYSICS

MARGARIDA TABORDA ANTÓNIO

BSc in Biomedical Engineering

DEVELOPMENT OF A FLEXIBLE SENSOR THROUGH ADDITIVE MANUFACTURING FOR MONITORING THE PROGRESSION OF PARKINSON'S DISEASE

MASTER IN BIOMEDICAL ENGINEERING

NOVA University Lisbon
September, 2024

NOVA SCHOOL OF SCIENCE & TECHNOLOGY

DEPARTMENT OF PHYSICS

DEVELOPMENT OF A FLEXIBLE SENSOR THROUGH ADDITIVE MANUFACTURING FOR MONITORING THE PROGRESSION OF PARKINSON'S DISEASE

MARGARIDA TABORDA ANTÓNIO

BSc in Biomedical Engineering

Adviser: Henrique Vazão de Almeida
Assistant Researcher, NOVA School of Science and Technology

Co-adviser: João Oliveira
Full Professor, NOVA School of Science and Technology

Examination Committee

Chair: Susana Isabel dos Santos Silva Sério Venceslau
Associate Professor, NOVA School of Science and Technology

Rapporteur: Ana Isable Bento Rovisco
Assistant Researcher, NOVA School of Science and Technology

Adviser: Henrique Vazão de Almeida
Assistant Researcher, NOVA School of Science and Technology

MASTER IN BIOMEDICAL ENGINEERING

NOVA University Lisbon
September, 2024

Development of a Flexible Sensor Through Additive Manufacturing for monitoring the progression of Parkinson's Disease

This document was created with the (pdf/Xe/Lua)LaTeX processor and the NOVAthesis template (v7.1.27) [1].

Para a Anita e para a Leninha.

Acknowledgements

Porque acredito que as pessoas com quem nos cruzamos influenciam o caminho que seguimos, deixo o meu agradecimento a todos aqueles a quem este final de ciclo também se deve.

Em primeiro lugar, gostaria de agradecer aos meus orientadores, Professor Henrique Almeida e Professor João Oliveira, por me terem dado a oportunidade de desenvolver um tema tão desafiante e do meu especial interesse. Obrigada por toda a ajuda, pela preocupação acerca do nosso bem estar e pela motivação que sempre transmitiram. Obrigada ao Rui por toda a ajuda e um obrigada muito especial à Maria que, para além de ter sido uma ajuda incansável e fundamental em todas as fases da dissertação, fez com que todos os dias saísse do laboratório a saber um pouco mais. Agradecer também a toda a equipa do CENIMAT | i3N que se cruzou comigo e, principalmente, à Sara. A sua companhia e o seu "vai dar certo" foram imprescindíveis no decorrer destes longos, e ainda assim rápidos, meses.

Obrigada às minhas amigas de sempre, Carolina J., Carolina P., Laura e Teresa. Às amizades para a vida que biomédica proporcionou, Inês M. e Joana, e à Mafalda, a amizade que a faculdade permitiu retomar. Um obrigada ainda mais especial à Inês L., amiga de sempre e amiga da faculdade. Tudo foi mais fácil por te ter como parceira de todas as horas. Ter encontrado amigas como vocês é uma alegria e um orgulho enorme. Que celebremos para sempre as conquistas umas das outras.

À família da faculdade, madrinha Bárbara, que me guiou desde o primeiro dia, e à minha afilhada Beatriz, por confiar em mim. E a todas as outras amizades criadas na faculdade e em Oldenburg, muito obrigada.

Agradeço ao João, por ser o meu conforto, a minha calma e segurança. Que continuemos a crescer juntos.

Obrigada à minha família, os meus maiores apoiantes e o meu apoio de todos os dias. Ao meu pai, que me fez perceber o privilégio e a importância de ter uma educação. Ao meu irmão, pessoa mais inteligente da família, por nunca duvidar de mim. À minha avó, a minha grande inspiração, e ao meu avô, que sei que estaria orgulhoso. Por fim, obrigada à minha mãe, por acreditar em mim como eu nunca acreditei. Tudo o que te devo e o que

tenho para te agradecer também dariam uma longa dissertação. Prometo-te não desitir dos meus sonhos.

Abstract

According to the World Health Organization, Parkinson's Disease (PD) affects a significant portion of the population (about 10 million, nowadays) and is expected to rise in prevalence over the years. Bradykinesia (slowness of movements) and tremor are the first indicators of the disease, and assessing these symptoms is crucial to understanding both Parkinson's Disease progression and the effectiveness of the treatment. However, nowadays, this assessment is made based on subjective criteria, such as the Unified PD Rating Scale, which rates these symptoms from 0 (no symptoms) to 4 (severe symptoms). This can lead to misinterpretations, causing inaccurate conclusions, resulting in the progression of the disease due to mistreatment. In this scope, a pressure sensor by additive manufacturing is developed for an objective assessment of PD symptoms and progression. The sensor is based on the triboelectric and piezoelectric effects to detect and measure finger movements (such as frequency and force) without requiring an external power source. The first step of the research included the design of the sensor, during which various active layer patterns were tested, and it was observed that smoother designs resulted in a higher output. This process was followed by the optimization of the prototypes' 3D-printing parameters, as well as the synthesis conditions of zinc oxide (ZnO) in the sensors' active layer to increase their sensitivity by coupling the tribo and piezoelectric effects. Subsequently, the performance of the sensors was analyzed under varying impact forces (30 to 60 N) at 2 Hz. ZnO was synthesized through a thermal bath at 60 ºC and its presence proved to double the output voltage generated upon an impact. The optimized process was used to develop two final prototypes: one designed for finger-tapping (FT) testing and the other for tremor detection, two widely used tests for PD monitoring. The final prototype exhibited the ability to accurately assess the FT test and detect tremor, suggesting that this device can be a promising, cost-effective and easily tailorable alternative to current assessment methods for tracking PD progression.

Keywords: Parkinson's Disease, Finger Tapping Test, Triboelectric Effect, Piezoelectric Effect, Additive Manufacturing

Resumo

Segundo a Organização Mundial de Saúde, a Doença de Parkinson afecta uma parte significativa da população (cerca de 10 milhões, actualmente) e prevê-se que a sua prevalência aumente ao longo dos anos. A bradicinesia (lentidão de movimentos) e o tremor são os primeiros indicadores da doença, sendo que a avaliação destes sintomas é crucial para compreender a progressão da doença e a eficácia do tratamento. No entanto, hoje em dia, esta avaliação é feita com base em critérios subjetivos, como a Escala Unificada de Avaliação da Doença Parkinson, que classifica os sintomas de 0 (ausência de sintomas) a 4 (sintomas graves). Este método de avaliação pode levar a interpretações erradas, resultando em conclusões imprecisas, que podem causar a progressão da doença devido à implementação de tratamentos inadequados. Esta dissertação visa desenvolver um sensor de pressão através de fabrico aditivo para uma avaliação objetiva dos sintomas e progressão da doença. O sensor baseia-se nos efeitos triboelétrico e piezoelétrico para detetar e medir movimentos dos dedos (como a frequência e a força), não sendo necessária a utilização de uma fonte de energia externa. A primeira etapa do desenvolvimento incluiu o design do sensor, durante o qual foram testados vários padrões de camadas ativas, e observou-se que designs mais suaves resultam numa maior tensão gerada. Este processo foi seguido pela otimização dos parâmetros de impressão 3D dos protótipos, bem como das condições de síntese do óxido de zinco (Zno) na camada ativa dos sensores, no sentido de aumentar a sua sensibilidade através do acoplamento dos efeitos triboelétrico e piezoelétrico. Posteriormente, foi analisado o desempenho dos sensores sob várias forças de impacto (30 a 60 N) e com uma frequência de 2 Hz. O ZnO foi sintetizado através de um banho térmico a 60 ºC e a sua presença resultou numa tensão de saída gerada aquando do impacto duas vezes superior. O processo otimizado foi utilizado para desenvolver dois protótipos finais: um deles concebido para o teste de batidas do dedo e outro para deteção de tremores, dois testes amplamente utilizados na monitorização de doença. O protótipo final exibiu a capacidade de avaliar com precisão o teste de batidas do dedo e detetar o tremor, sugerindo que este dispositivo pode ser uma alternativa promissora, económica e facilmente adaptável aos métodos de avaliação atuais para monitorizar a progressão da Doença de Parkinson.

Palavras-chave: Doença de Parkinson, Teste de Batidas do Dedo, Efeito Triboelétrico, Efeito Piezoelétrico, Fabrico Aditivo

Contents

List of Figures

List of Tables

Acronyms

AM Additive Manufacturing *(p. 3)*

CAD Computer-Aided Design *(pp. 2, 3, 14)*
CF Conductive Filaflex *(pp. xi, xiii, 14, 16, 18–20, 22–31, 36, 38)*

DSC Differential Scanning Calorimetry *(pp. 27, 31, 32)*

FDM Fused Deposition Modeling *(pp. 3, 16)*
FT Finger Tapping *(pp. xi, xiii, 2, 10–14, 20, 27–29, 39, 41)*

LIG Laser-Induced Graphene *(pp. xi, xiii, 9, 14–16, 19, 21, 24–27)*

MDS-UPDRS Movement Disorder Society-sponsored revision of the Unified Parkinson's Disease Rating Scale *(pp. 1, 10–12)*
MRS Micro-Raman Spectroscopy *(pp. xii, 14, 21, 36)*

OV Output Voltage *(pp. 6, 12, 13, 16, 26–30, 36–39)*

PCB Printed Circuit Board *(p. 12)*
PD Parkinson's Disease *(pp. xiii, 1, 2, 10–12, 40)*

SD Standard Deviation *(pp. 25, 37–39)*
SEM Scanning Electron Microscopy *(pp. xi, xii, 14, 28, 32–34, 56, 57)*

TECD Triboelectric Charge Density *(pp. 6, 63)*
TPU Thermoplastic Polyurethane *(pp. xi, xiii, 7, 14–16, 18–29, 31–35, 37–41)*

XRD X-Ray Diffraction *(pp. xi, 14, 24, 28, 32, 34)*

Symbols

ρ Resistivity *(p. 25)*

ρ_s Resistance *(p. 25)*

t Thickness *(p. 25)*

1 Introduction

The following work was developed within the scope of the Master's Dissertation in Biomedical Engineering and aims to produce a 3D-printed sensor to objectively assess the Finger Tapping Test in PD patients.

1.1 Motivation

According to the World Health Organization, the prevalence of PD has doubled in the past 25 years and global assessments in 2019 revealed that more than 8.5 million individuals were affected by the disease [2]. It particularly affects individuals over 50 years old, and as age increases, so does the number of diagnoses and symptoms of Parkinson's Disease. By 2040, the number of patients diagnosed with the disease is expected to increase to over 17 million [3, 4].

PD is a chronic neurodegenerative disease that is characterized by the decrease of dopamine, a neurotransmitter that acts in the transmission of signals between nerve cells [5]. This leads to motor symptoms such as tremor, bradykinesia (slowness of movements), muscle stiffness and imbalance [6, 7].

The diagnosis of PD relies on clinical criteria such as rating scales and the manifestation of symptoms like the ones mentioned earlier. A neurology specialist is responsible for making the diagnosis and monitoring the disease's progression, scheduling visits every six to nine months [8]. During a patient's examination, the neurologist runs specific physical tests like finger and foot tapping, as well as pronation or supination hand movements [4, 9].

Monitoring the disease typically involves semi-quantitative rating scales to measure its progression, like the Movement Disorder Society-sponsored revision of the Unified Parkinson's Disease Rating Scale (MDS-UPDRS) [4, 10, 11]. There are 4 parts of the MDS-UPDRS: Part I corresponds to the patient's "non-motor experiences of daily living"; Part II concerns "motor experiences of daily living"; Part III is related to "motor examination" and Part IV corresponds to "motor complications" [12]. The MDS-UPDRS Part III is focused on evaluating motor symptoms [4, 12, 13], requiring patients to perform some tasks in order

to assess tremor and bradykinesia. The evaluation is made based on a 5-point scale from 0 to 4 that corresponds to no symptoms, slight, mild, moderate and severe symptoms, respectively [4, 12, 13]. Nevertheless, employing a rating scale during semi-annual clinical examinations may have limitations [8, 14]. Even though healthcare practitioners have standardized training to apply the scale, the assigned scores may vary, introducing intra-rater and inter-rater variability. This variability can cause errors, impacting the test's reliability and reproducibility [4].

The subjective rating scales, coupled with the infrequency of these assessments and the variation of symptoms between days and even throughout the patient's daily life, can introduce potential errors in evaluating the progression of the disease [4, 8, 14, 15]. Alternative or supplementary assessment methods may be beneficial for a more comprehensive and reliable understanding of the disease's evolution [4, 15].

Given that the assessment of symptoms and disease progression is crucial for the effective management of PD [4], the implementation of the 3D-printed sensor proposed in this work could play a significant role during clinical appointments. Its potential to enhance the accuracy of tracking disease progression and provide valuable insights into the patient's overall well-being makes it a valuable tool in managing the disease.

1.2 Central Aims

This thesis aims to fabricate a 3D-printed device based on the coupling between the triboelectric and piezoelectric effects.

The main goal is to create a device with the ability to quantify the FT test, able to give information about the velocity, frequency and force of movements, which will provide relevant information about both the progression of PD and the efficacy of the medication [16]. The device was designed using a CAD software and manufactured through 3D printing, ensuring a cost-effective alternative that can be customized to individual patient's needs. The sensor's working principle relies on the triboelectric and piezoelectric effects. Tribo/Piezoelectric sensors have been widely explored for pressure monitoring as they present a straightforward production process and simple working principles [17].

The proposed sensor stands out from alternatives, in particular, devices with built-in accelerometers, as it does not need an external power source to operate and can be easily customized. It is worth highlighting the possibility of easily adapting the geometry of the sensor in order to enhance its performance or adapt it to the user. In this way, the proposed method is a simple and cost-effective custom-made alternative for monitoring PD.

The research work described in this dissertation was carried out in accordance with the norms established in the ethics code of Universidade Nova de Lisboa. The work described and the material presented in this dissertation, with the exceptions clearly indicated, constitute original work carried out by the author.

2

Theoretical Concepts

In this chapter, some crucial theoretical concepts will be presented to provide an understanding of the sensor fabrication process and the underlying concepts related to its operating principle.

2.1 Additive Manufacturing

Additive Manufacturing (AM) is a technology with the ability to take the information from a CAD file that was later converted into a stereolithography (STL) file (which approximates the previous design into triangles) and print each layer of information [18]. AM entails countless advantages when compared to conventional processing methods: it allows the production of complex geometries with almost no need for post-processing, materials such as polymers and metals can be used, and it has near-zero material waste. Therefore, AM is environmentally and economically promising [19]. This technology is based on incrementing layer-by-layer manufacturing, but different methods can be used according to the final piece to be manufactured and its intended properties [20]. There are several AM alternatives, as shown in Figure 2.1, but the most used approach uses powder or wire as a feedstock that is selectively melted by a focused heat source and later consolidated by cooling [20].

Fused Deposition Modeling (FDM) has become one of the most widely-used AM methods. In this process, a filament is fed through a heated element and becomes molten. Then, the filament is fed through a nozzle and deposited onto the partially constructed part. According to the final geometry, the head moves on the X-Y plane and deposits material. When a layer is finished, the platform moves vertically in the Z direction and starts depositing another layer on top of the previous one. This method allows the use of thermoplastic materials, such as acrshortabs (acrylonitrile butadiene styrene), acrshortpc (polycarbonate), acrshortpla (polylactide), acrshorttpu (thermoplastic polyurethane), and the possibility of combining them with ceramic or metallic powders [18, 21].

3D-printed devices based on the triboelectric effect have been developed over the years, using materials such as PDMS (polydimethylsiloxane) and PLA.

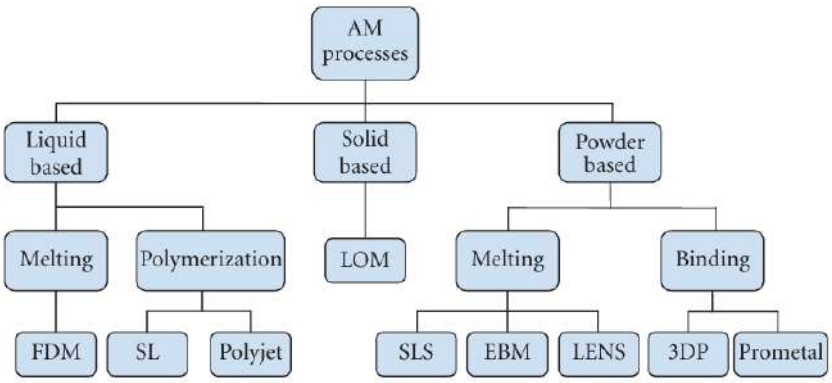

Figure 2.1: 3D Printing Processes. Adapted from Wong *et al.* (2012)[18]. LOM (laminated object manufacturing), SL (stereolithography), SLS (selective laser sintering), EBM (electron beam melting), LENS (laminated engineered net shaping)

2.2 Triboelectric Effect

The triboelectric effect occurs in the presence of two different materials. The interaction between these two materials should provide the donation of electrons by one of them and the reception of electrons by the other [22]. Triboelectrification is the term used when electric charges at the contact surface of the materials are generated through friction [23].

In a triboelectric device, opposite electric charges will be induced by the contact between the two layers of materials under an external mechanical compressive force. Based on the materials' tendency to donate or accept electrons (according to their electron affinity), a triboelectric hierarchy series has been developed. When two materials from opposite sides of the table contact with each other, electrons are moved from one of the materials (donor) to the other (acceptor).

Triboelectric sensors use the triboelectric effect to detect changes in physical properties like pressure or motion [23]. Thus, triboelectric sensors convert a mechanical signal into an electrical signal [24]. A sensor based on the triboelectric effect can have one of four working principles (Figure 2.2): the vertical contact separation mode, the lateral sliding mode, the single electrode mode and the freestanding triboelectric-layer mode.

2.2.1 Vertical Contact Separation Mode

In this mode, the two materials come into contact and then separate vertically. The direct contact between the materials results in the development of opposite charges, influenced by their respective electron affinities [25]. When the external force is released, the distance between the materials increases and a potential difference creates an electron flow in the circuit, as a result of the electrostatic induction effect. As soon as the two materials are fully separated, a net energy balance occurs. On the other hand, as the separation between the materials gradually decreases once more, prompted by an external compression force, electrostatically induced charges flow in the opposite direction, generating a reverse

electric current (negative cycle). Consequently, the contact and subsequent separation of the triboelectric materials through the compression force result in the production of a positive–negative alternating current cycle [23].

2.2.2 Lateral Sliding Mode

This mode involves the lateral sliding or rubbing of two materials with different triboelectric properties against each other. When the two layers contact, there are opposing charges being generated. In the beginning, there is an equal and opposite charge density between the two layers, but as the top layer slides outward proportionally to the base layer, it creates dislocated areas in the sliding direction and the triboelectric charges are not fully compensated, which creates an electrical charge at the surface of each material. This leads to a flow of electrons from the bottom to the top electrode until the top layer slides out entirely. This back-and-forth movement generates an electric drop induced by the flow of electrons across the top and base electrodes and output can be detected [25].

2.2.3 Single Electrode Mode

This mode is characterized by having only one electrode, and the opposing contact layer lacks any connections. It consists of one moving layer and one grounded electrode layer. When the first layer undergoes movement, it induces a change in the local electrical field distribution, initiating a flow of electrons between the two layers to equalize the potential difference. This mode is capable of operating in both vertical and lateral sliding modes [25].

2.2.4 Freestanding Triboelectric-layer Mode

In this mode, the moving layer is not attached to any electrodes or wires. It is composed by two symmetric electrodes and a dielectric layer of the same order in size. The electrodes are positioned beneath the dielectric layer, maintaining a small separation, and another small gap is kept between the electrodes. The dielectric layer undergoes pre-charging through the triboelectric process. Asymmetric charge distribution occurs as a result of the relative movement between the layer and electrodes. The potential generated due to these asymmetric charges is counterbalanced by the flow of electrons from one electrode to another, resulting in an alternating current output. This mode is well-suited for self-powered vibration sensors.

The performance of the triboelectric sensor is dependent not only on its operating mode, but also on the materials present in its composition. As so, it is essential to carefully study the materials to use.

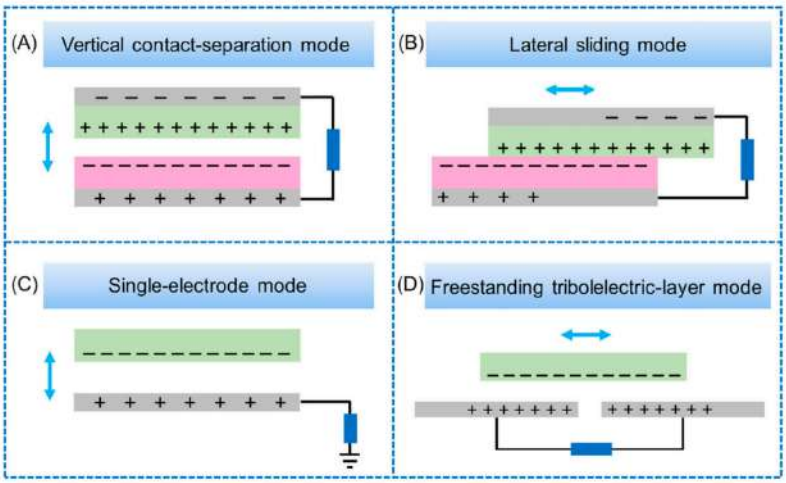

Figure 2.2: Different Modes for Sensors Based on the Triboelectric Effect. (A) Vertical Contact-Separation Mode. (B) Lateral Sliding Mode. (C) Single Electrode Mode. (D)Freestanding Triboelectric-Layer Mode. Adapted from Zhao *et al.* (2024) [26].

2.2.5 Triboelectric Materials

As referred previously, it is necessary to have two materials with different triboelectric properties to generate an electrical output upon contact between the materials. The output voltage (OV) of a device based on the triboelectric effect is determined by the materials present in its architecture. In this scope, the triboelectric series is a fundamental tool as it lists different materials depending on their electron affinity. A triboelectric series ranks different materials taking in account their tendency to lose or gain electrons, which can be measured by using the normalized triboelectric charge density (TECD) [27]. Zou *et al.* [27] measured the TECD of different materials based on their triboelectrification with mercury operating with the contact separation mode. If the tested material was negatively charged after contacting with mercury, the TECD was recorded as a negative value. On the other hand, if the material is positively charged after contacting with mercury, the TECD is recorded as a positive value. The materials that were tested and their TECD are listed in Annex I. For each material, when $\alpha > 0$, the material tested was more positive than the reference liquid (mercury) that was used in all tests. On the other hand, if $\alpha < 0$, then the material is more negative than the reference. α represents the normalized triboelectric charge density.

Based on the triboelectric series, it is possible to evaluate which pair of materials will produce a higher output signal, as the latter is proportional to the distance in the series [28]. Figure 2.3 shows the relative position of different materials, according to their tendency to lose or gain electrodes.

When analyzing Table I.1 (Annex I), it is possible to conclude that polymers present high average TECD, which might explain their frequent use as triboelectric layers [29]. Besides high TECD, polymers also present flexibility, elasticity, lightness and conformability, which make them interesting materials to include in the sensor to be developed in the scope of

this thesis. Among the different polymers, TPU was chosen due to its remarkable flexibility, mechanical properties, biocompatibility, ease of processing, durability and adaptability, making it highly suitable for applications requiring long-lasting and adaptable materials.

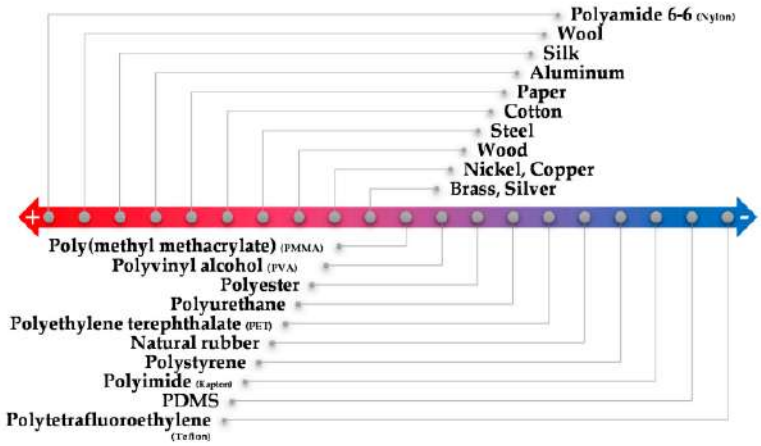

Figure 2.3: Triboelectric Series. Adapted from dos Santos *et al.* (2020) [30].

The piezoelectric effect is an electrical phenomenon that can be coupled with the triboelectric effect to maximize the output voltage of a sensor.

2.3 Piezoelectric Effect

The piezoelectric effect generates electrical potential in a material when an external stimulus is applied. It happens in certain materials, particularly the ones that have a non-central symmetry. The external stimuli create displacements of dipoles within the material, thus creating the piezoelectric potential [31, 32].

In a monocrystal, the polar axes of all the dipoles lie in one direction, whilst in a polycrystal, different regions within the material have different polar axes [32].

When the material is at rest, the positive and the negative charges within the material balance each other, the electric dipoles cancel each other and, in this case, there is no electrical output. On the other hand, if an external force is applied, the material will suffer changes in the relative position of the atoms in relation to each other and, consequently, of the dipoles. This leads to a change in the dipole mode and the charges do not cancel each other, which results in a potential difference within the material. In this case, there is a tendency for positive charge to accumulate at one end of the material and negative charge at the other end. The potential difference generated leads to the movement of charges in an external circuit, which generates a measurable electrical signal [33].

Piezoelectric Sensors use the piezoelectric effect in order to convert mechanical stimuli into electrical signals [24, 34].

The piezoelectric effect has been used to develop devices that actuate to control tremor [35–37]. Hybrid devices (using both piezoelectric and triboelectric effects) have proved

that this combination can be used to improve the output signal [38, 39].

2.3.1 Piezoelectric Materials

Ceramics, crystals and polymers are classes of materials that present piezoelectricity [33].

Among the several piezoelectric materials, such as quartz, barium titanate, zinc tin oxide, ZnO stands out as an interesting alternative.This is primarily due to its simple and cost-effective production process, non-toxicity, and suitability for nanostructured applications, making it a highly versatile, safer, and more sustainable option compared to other materials [40, 41].

2.3.1.1 ZnO as a Piezoelectric Material

ZnO is environment-friendly and biocompatible. This metal oxide can be synthesized in different morphologies through cost-effective and time-effective approaches with good repeatability and reasonable yield [42].

ZnO has a crystalline hexagonal wurtzite structure (B4) where the Zn^{2+} cation is surrounded by four O^{2-} anions [41, 43]. This structure, shown in Figure 2.4, is what allows the material to generate piezoelectricity. When ZnO suffers an impact, a displacement between the cation and the anions occurs, leading to an electrical charge redistribution that establishes an electric dipole and creates a potential difference [44].

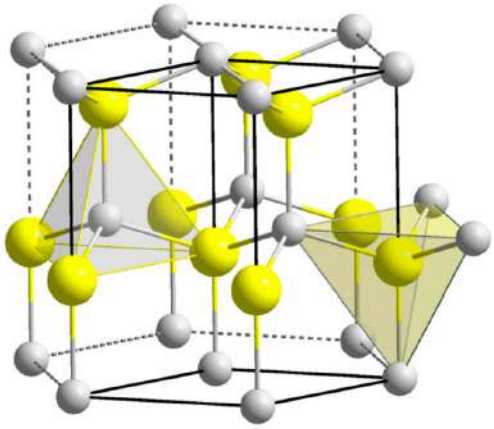

Figure 2.4: ZnO's Crystalline Hexagonal Wurtzite Structure. Adapted from Borysiewicz *et al.* [45].

ZnO's piezoelectricity has led to its use in the development of devices such as sensors based on the piezoelectric effect [40, 41, 46]. It can be synthesized through several procedures like radio frequency sputtering, thermal deposition, chemical vapor deposition, spray pyrolysis, sol-gel, hydrothermal and chemical bath process [41].

ZnO can have different structures based on the size and morphology like nanocolumns, nanowires, nanosheets, nanofibers, nanoflowers, nanoparticles, quantum dots, nanobelts, nanoneedles or nanorods, depending on its processing methods [45, 47].

The hydrothermal method is a simple and low-cost process that allows the growth of ZnO nanostructures while coating a large substrate area using a relatively low temperature (under 95 °C) [41].

Triboelectric and piezoelectric materials are the fundamental parts of the sensor's active layer. However, another critical component to consider is the device's electrodes.

2.4 Electrode Materials

Conductive materials are crucial components that influence sensor's performance. Recently, research about flexible force sensors has been developed, which boosted the use of conductive materials that are also flexible [48]. The use of metal nanomaterials, carbon materials and transition metal carbides (like MXenes) has been reported [49, 50]. Carbon materials have the advantage of being environmentally and biologically friendly.

2.4.1 Laser-Induced Graphene

Graphene is a carbon-based material and its properties, production methods and applications have attracted a wide research interest [51–53].

Laser-Induced Graphene (LIG) represents a significant advancement in the production of graphene-based materials, offering a versatile and scalable approach to generating three-dimensional porous graphene structures. Unlike traditional methods such as chemical vapor deposition and wet-chemical processes, which require high temperatures, pure gases, and potentially hazardous chemicals, LIG is formed through a one-step laser irradiation process [52, 53]. This method typically involves using a commercial CO_2 infrared laser system. The properties of LIG can be finely tuned by adjusting the laser parameters, such as power, pulse width, and spot size, which influence the thickness, conductivity, and porosity of the resulting graphene [52]. LIG is characterized by its unique "kinetic" structure, where the graphene lattice includes a mix of hexagon, pentagon, and heptagon rings, a result of the fast cooling during laser processing [52, 54].

Polymeric substrates like polyimide are commonly used to engrave LIG, but other organic materials have also emerged as viable alternatives, such as wood [52] and even paper [55].

LIG on a paper substrate can also be separated from the paper and transferred to other flexible substrates. Pinheiro *et al.* [55] developed a technique that enables the water-based peel-off of LIG from paper, facilitating its efficient transfer to various substrates.

The scalability and simplicity of LIG production, combined with its adaptability to various materials, position it as a promising material for future technological applications, including energy storage devices and sensors. Moreover, LIG is an attractive material to be used in several research areas that require efficient, cost-effective, and versatile graphene-based solutions.

3

State of the Art

In this chapter, a comprehensive literature review will be conducted, focusing on existing sensors developed for FT evaluation in PD and other neurodegenerative diseases, as well as the explanation on how the FT exam's procedure is done nowadays. Different sensors and the corresponding working principles will be described in detail and a list of the materials used to produce these sensors will be presented.

3.1 Finger Tapping Evaluation

The Finger Tapping Test is one of the motor examinations usually tested on patients with neurodegenerative diseases like Parkinson's or Alzheimer's and is included in the MDS-UPDRS [56]. It is used to evaluate the patient's range of motion, fine motor skills, bradykinesia [57] and medical treatment's efficiency [57, 58]. The test involves patients tapping their index finger against their thumb as quickly as possible for 10 seconds, while keeping their fingers spread as far apart as possible between each tap [56, 58–60]. The evaluation of the exam is made by a specialist who, based on the observation of the exam and relying on MDS-UPDRS scaling rates, will quantify it on a scale from 0 to 4, like it was explained in Section 1.1. It is expected that, comparing with healthy individuals, PD patients' movements will become slower and shorter in amplitude with each time repetition [61].

3.1.1 Devices for Quantitative Assessment of Finger Tapping

Over the years, some devices have been developed with the aim of assessing and quantifying the finger tapping test, most of them making use of inertial sensors.

Romero *et al.* [62] developed a 3D-printed small, lightweight, strong and ergonomical device made of PLA that could incorporate an inertial sensor with the aim of quantitatively identifying and monitoring bradykinesia. This device measured the frequency of the FT movements in patients with PD before and after receiving their normal levodopa treatment and it was capable of detecting a maximum frequency in the range of 0.1 to 4.3 Hz. In the end, it was concluded that, after the medication was administered, there was a decrease in

the frequency of the movement, which suggests a positive influence of levodopa, allowing patients to improve their motor control and dexterity.

Also recently, Ravichandran *et al.* [63] designed a glove that allows in-home evaluation of patients. This system consists of two textile gloves with flexible sensors incorporated in the fingers, an inertial measurement unit and a microcontroller unit. It assesses PD symptoms such as tremor, bradykinesia and fine motor movements through the performance of MDS-UPDRS Part III exercises, like the FT test. Data is acquired wirelessly, and the gloves (one in each hand) are connected to a custom tablet. The results of a pilot study demonstrated the device can successfully collect movement data and differentiate between pre- and post-medication states in most participants.

Other approaches using everyday technology, such as smartphones [64], smartwatches [15, 65] and videos [66], have also proved to be effective in assessing the symptoms of the disease. Machine learning algorithms have been increasingly used in PD data analysis [4, 66, 67].

Table 3.1 shows an overview of the devices developed to quantify symptoms in patients with PD who were tested for the FT test.

Table 3.1: Quantitative Assessment of Symptoms in Patients with Parkinson's Disease.

Measure System	**Symptom**	**Parameters Measured**	**Ref.**
Accelerometer, Touch Sensor	Bradykinesia	Rythm, Amplitude, Velocity	[68]
Inertial Sensor	Bradykinesia	Frequency	[62]
Flex sensor Inertial Sensor	Tremors, Dyskinesias and Bradykinesia	Frequency, Amplitude. Energy	[63]
Accelerometers, Force Sensors, Touch Sensors	Tremors, Bradykinesia, Rigidity	Frequency, Amplitude, Force, Time Movement	[69]
Leap Motion Controller, Accelerometer, Gyroscope	Bradykinesia	Frequency, Amplitude Angle	[67]

By analyzing Table 3.1, it is possible to conclude that most of the devices developed use inertial sensors (accelerometers and gyroscopes) as their measurement system. Frequency and amplitude are the most commonly measured parameters using these devices.

3.1.2 Finger Tapping Devices Based on the Triboelectric and/or Piezoelectric Effects

Vera *et al.* [70] developed a flexible forearm triboelectric sensor that aims to help in diagnosing and monitoring PD. The triboelectric materials used were Ecoflex and PEDOT:PSS and the sensor working principle was the contact-separation mode. An aluminum film was bonded to PEDOT:PSS and used as the electrode. This setup allows signal observation by connecting a measurement circuit through a wire attached to the aluminum film. A bluetooth low energy (BLE) board was also used. A small, printed circuit board (PCB) was

attached to the Ecoflex layer, responsible for processing and transmission of the signal. The PCB had a conditioning circuit with filtering and amplification stages. Subsequently, the signal was digitized by an Analog-to-Digital Converter within one of the input channels of the BLE module, which then wirelessly transmitted the data to a computer [71]. The device was placed above muscles and tendons that control fingers, hand and wrist movement, located in the forearm. The sensor quantified specific movements that are also required in the MDS-UPDRS like finger tapping, pronation/supination and hand opening/closing. The developed reading and processing circuit allowed to monitor bradykinesia and tremor. Regarding the FT test, different OV was registered according to which finger was used and the different levels of the MDS-UPDRS rating scale were being emulated. Concerning the tremor evaluation, it showed that when the tremor amplitude increased, the voltage also increased with an alternating waveform so that the output signal was correlated with the wrist motion in amplitude and frequency.

Haque *et al.* [72] fabricated a contact-separation mode triboelectric sensor using 3D-printed functional layers. TangoBlack and PDMS were 3-printed through multi-jet modeling and direct ink writing, respectively, and used as active layers. Carbon black particles were dispersed into PDMS and polyurethane, fabricating electrically conductive materials that were used as electrodes. A spring structure made of polyamide was also 3D-printed to create a wider gap between the charges' affinities, enhancing the sensor's performance. The sensor was assembled and its impact response to FT was studied (with a force of approximately 22 N), presenting a peak-to-peak voltage of 197.4 V for a frequency of 1 Hz and 253 V for 2 Hz. Its response to different active sensing areas, forces and frequencies was also tested. It was also possible to conclude that TangoBlack has a positive charge affinity similar to polyurethane.

Relating to the development of triboelectric and piezoelectric sensors based on ZnO structures synthesized through chemical bath deposition of ZnO structures, Kumbhakar *et al.* [73, 74] and Patnam *et al.* [39] proved its effectiveness in tapping tests.

Kumbhakar *et al.* [73] developed a 3D-printed structure made of PLA that was immersed in a zinc salt and NaOH solution, for the growth of ZnO nanosheets on the polymer surface. This device showed a stable interface, enhanced charge transfer and performance and its structure exhibited flexibility, strong adhesion and tunable surface area. The electrostatic interaction between 2D ZnO and the PLA polymer generated a piezopotential inside the materials in response to an externally applied compressive force which makes the developed sensors a valuable alternative for developing wearable sensors. The structure was blended, twisted, stretched and tapped. The FT movement proved to be the one that created a higher peak-to-peak voltage of about 3.25 V.

Table 3.2 presents a general review of triboelectric and/or piezoelectric devices that were not only tested for FT, but whose functional mechanism could be used to test it in patients with PD.

Table 3.2: Triboelectric and/or Piezoelectric Devices that Could Be Used for FT Test.

Application	**Active Layer**	**Electrode**	**OV for FT (Peak-to-Peak)**	**Dimension (cm^2)**	**Ref.**
Flexible Forearm Triboelectric Sensor	PEDOT:PSS, Ecoflex	Aluminum	1.9 V	3.5×4	[70]
3D-Printed Sensor Using ZnO Nanosheets	ZnO, PLA	-	3.25 V	5×5	[73]
Piezo/Triboelectric Nanogenerator for Sensing Applications	Y-ZnO PDMS	Aluminum	80 V	2×2	[39]
Triboelectric Touch Sensor	PDMS, TangoBlack	CPDMS, CPU	197.4 V (1 Hz) 253.0 V (2 Hz)	9	[72]
Triboelectric Tactile Sensing	PDMS	Ag Nanowires	1.11 V	7.5×7.5	[75]
Flexible Piezoelectric Tactile Sensor	PVDF	Aluminum	4.2 V	1.5	[76]
Piezoelectric Polymer Sensor Pad for Finger Tap Analysis	PET PVDF-ZrO_2	Aluminum	115 mV	1.5×1.5	[77]
Ultra-stretchable Triboelectric Nanogenerator for Tactile Sensing	TPU	AgNWs/rGO	20 V	2×2	[78]

Table 3.2 shows that the most flexible material used in the development of the devices was TPU, while the electrodes were mainly aluminum and silver. The peak-to-peak voltage ranged from 1.9 V to 253 V and the dimensions ranged from 1.5 cm^2 to 9 cm^2. However, there is no correlation between these two parameters, given that different materials were used, as well as different impact forces.

4

Materials and Methods

This chapter presents the materials and methods used to fabricate the sensors to be used in the FT test and to monitor tremor. The developed sensors will be based on both the triboelectric and piezoelectric effects, having an active layer of TPU/ZnO and working as a single electrode mode. A chemical characterization of the conductive filament was performed through Micro-Raman Spectroscopy (MRS) and a structural characterization through X-Ray Diffraction (XRD) to determine its conductive substance. A morphological characterization of the samples subjected to the ZnO growing process was performed using Scanning Electron Microscopy (SEM). The electrical characterization of the materials used as electrodes was conducted through sheet resistance evaluation.

4.1 Conductive layer

In order to measure a signal from the sensor, it is necessary to have a conductive layer, which acts as the electrode. Being the active layer of this sensor composed of TPU, it is important to choose a material that, besides being conductive, can exchange electric charges with this polymer.

In this scope, carbon additives were reported to enhance the performance of triboelectric devices [28, 79]. Thus, carbon tape was initially used as an electrode to test the sensors, as it provided a simple and cost-effective method for producing an electrode. This approach allowed for assessing the feasibility of using carbon and TPU as a triboelectric pair. After being verified that these materials generated triboelectric response, other carbon-based materials, such as Conductive Filaflex (CF) and LIG, were tested as electrodes. Figure 4.1 shows the electrodes used.

4.1.1 Conductive Filaflex Electrode

A CF electrode was printed by Raise 3D and the CF filament was purchased on *R*ecreus [80]. The design was created through SolidWorks, a CAD software, and ideaMaker 5.0.6. was used to slice the design and convert the STL file (originated from SolidWorks) into a

sliced file, compatible with the printer. The bed temperature of the printer was kept at 0 °C and the temperature of the extruder nozzle was 245 °C.

4.1.2 Laser-Induced Graphene Electrode

Initial tests to produce in-situ LIG on a 3D-printed TPU substrate were conducted using Laser System VLS3.50, a CO_2 laser with 10.6 μm, 50 W maximum power and 127 mm/s maximum scan speed. Squares of 2 × 2 mm^2 were sketched using Adobe Illustrator and engraved on TPU substrate. The substrate was directly placed on the equipment's table and the engraving occurred under a nitrogen flow. A combination of values of power and speed between 1% (corresponding to a power of 0.5 W and a 0.0127 m/s speed) and 30% (corresponding to a power of 15 W and a 0.3175 m/s speed) was tested. The pulses per inch (PPI) used was 1000 and the distance was kept constant at the focal point. However, a difference between these values of about 10% would originate a hole in the substrate. Neither the conditions tested led to the formation of LIG due to the low thermal resistance of the substrate. Therefore, a fire-retardant treatment of the TPU substrate was conducted. Pinheiro *et al.* [55] describes the treatment of paper with sodium tetraborate decahydrate as a fire retardant and a similar procedure was used for TPU. A 0.1 M sodium tetraborate decahydrate (Borax, $Na_2[B_4O_5(OH)_4]{\cdot}10H_2O$, 99%, 1303-96-4) aqueous solution was prepared, and a TPU sample was immersed in the solution for 2 hours under stirring. The TPU piece was first heated on a hot plate at 100 °C for 10 minutes with the aim of enhancing the adhesion of borax to the TPU. In the end, it was left drying at room temperature overnight. The chemically treated TPU was then irradiated using the combinations of power and speed that were previously tested. However, no LIG was formed.

Cheng *et al.* [81] and Cao *et al.* [82] demonstrated the LIG fabrication on a TPU substrate using a Nd: YAG laser irradiation machine with a 1064 nm wavelength. Therefore, the Laser System PLS6MW, a fiber laser of 1.06 μm was also used. The chemically TPU substrate was irradiated with this laser, using combinations of power and speed that were also tested on the first laser. However, none of these combinations among others that were tried, with parameters being increased step by step, resulted in the production of LIG. While the previous laser showed that a difference equal to or above 10% between the power and speed parameters would lead to a hole, the same was not verified using the fiber laser. Even conditions such minimum speed and maximum power that did not allow the fabrication of LIG on TPU, resulted in a substrate without any visible alterations.

Without being feasible to produce LIG directly on the TPU substrate following the previous procedure, a water peel-off transfer of paper-based LIG was done as described by Pinheiro *et al.* [53]. A previously chemically treated paper with borax as a fire-retardant was used as a substrate to produce LIG electrodes and was irradiated with the CO_2 laser. Paper was fixed to a glass support (ensuring a flat surface), rast mode was used, the PPI was set at 1000, the power and speed used was 12% (6 W and 0.1524 m/s, respectively) and the

distance between the laser beam and the substrate was -1.6 mm. The pattern intended to be laser engraved was a 2×3 rectangle with a coupled 2 cm diameter semicircle (as shown in images 4.1b, 4.1c and 4.1d) and it was also designed through Adobe Illustrator. Before the transfer, the samples that were 3D-printed with the purpose of being used as substrates for the LIG were sprayed with an adhesive spray and were left drying for 30 minutes. The paper transfer followed the following steps: first, both surfaces were submerged in water; then, the paper with LIG substrate was pressed against the 3D-printed sample (that was previously made adhesive) during 10 seconds; finally, the paper substrate was peeled off and the LIG pattern was attached to the 3D-printed substrate. Figure 4.1 shows all the electrodes developed and tested.

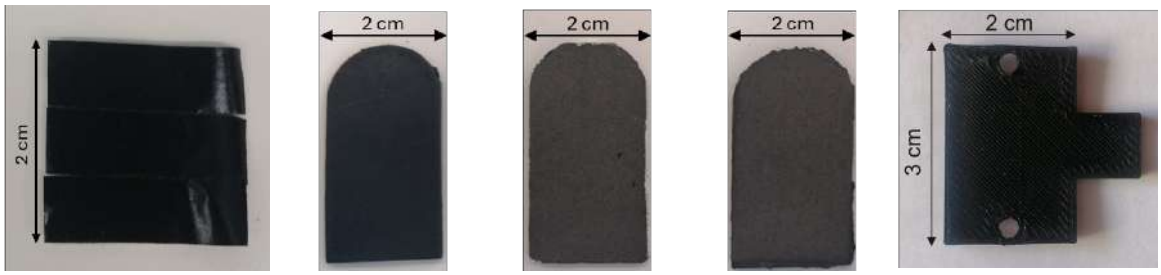

(a) Carbon Tape. (b) CF. (c) TPU w/ LIG. (d) CF w/ LIG. (e) CF for Attachment.

Figure 4.1: Electrodes Subjected to Different Impact Forces (between 30 N and 60 N).

4.2 Sensor Fabrication

A commercial polyurethane filament was chosen as an active layer of the triboelectric sensor to develop an adaptable and flexible device. The thermoplastic polyurethane (TPU 95A white) was purchased from *U*ltiMaker and the printer used was UltiMaker S3, a FDM-type 3D-printer.

The resistance of a triboelectric pressure sensor changes when a pressure is applied, which will change the sensor's OV. Thus, the pattern used, more specifically the pattern of the contact area, will influence this resistance and consequently the sensor's sensitivity [83]. According to what was used in literature to produce pressure sensors [83–86], patterns such as curves, cones, spheres, waves and hexagonal shapes were printed.

The different designs were also modeled through *S*olidWorks and UltiMaker Cura 5.6.0 was used to slice the design and convert the STL file into a sliced file, compatible with this printer. Different types of infill and printing speeds were tested in order to assess the best parameters to print each design. The bed temperature of the 3D printer was kept at 0 °C and the extruder temperature used was 225 °C.

Table 4.1 presents the designs produced, as well as the corresponding printing settings used. All the designs had a dimension of 20×20 mm^2 and a 2 mm base thickness.

Table 4.1: 3D-Printed Designs (the images depicted scale is 750 μm).

Design	Design Name	Protrusion Height	Space Between Protrusions	Infill	Printing Speed
	Square	-	-	15 %	35 mm/s
	Cones	1.5 mm	2 mm	15 %	15 mm/s
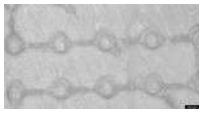	Spheres	1.5 mm	2 mm	15 %	20 mm/s
	Waves	2 mm	3mm	15 %	15 mm/s
	Archimedean Square	1 mm	0.5 mm	15 %	25 mm/s
	Circle	-	-	15 %	35 mm/s
	Archimedean Circle	1 mm	0.5 mm	15 %	25 mm/s
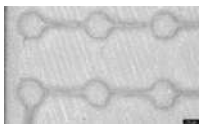	Hexagons	1.5 mm	2 mm	10 %	25 mm/s
	Hexagon Holes	1.5 mm	2 mm	15 %	25 mm/s

4.2.1 Synthesis of ZnO

ZnO was the material chosen to act as piezoelectric sensing element, as it is, as referred previously, biocompatible, environmentally friendly, non-toxic and can be synthesized through cost-effective and time-effective processes.

A similar procedure as Kumbhakar *et al.* [73] described was used to fabricate ZnO on a 3D-printed sample. First, sodium hydroxide (NaOH, 98% 1310-73-2) solution (3 M) was prepared and the 3D-printed structure was submerged in it for 2 hours, with the aim of increasing the roughness of the surface in order to stimulate ZnO growth. A Zinc Nitrate Hexahydrate ($Zn(NO_3)_2 \cdot 6H_2O$) solution (0.5 M) on a mixture of water in ethanol (EtOH:H_2O, 50/50) was prepared, as well as another solution of NaOH (30 mg/mL) and ethanol. The 3D-printed sample was immersed in the Zinc Nitrate solution and the second solution was added dropwise, increasing the pH until 10 was reached. Every step of the

procedure was done with the solution at 60 °C and it was kept at this temperature for 3 hours after a pH value of 10 was reached. Taking into account the ZnO structure, the 3D-printed design used was the "Hexagon Holes", so that the growing of ZnO nanosheets was promoted. Figure 4.2 summarizes the ZnO growing procedure.

The procedure described below was the one used for the final prototype. However, other conditions were also tested. Besides the "Hexagon Holes" design, the procedure of the ZnO growth was also tested using the "Hexagons" pattern. Moreover, for the "Hexagon Holes" pattern, the synthesis time and temperature were varied between 2 hours and 3 hours and 60 °C and 70 °C, respectively, in order to understand the influence of these parameters on the metal oxide growth.

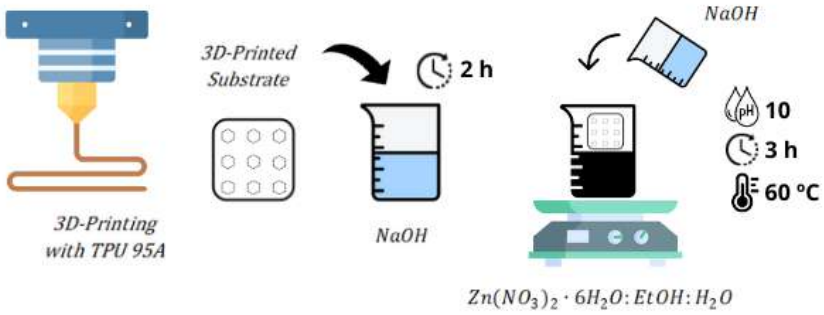

Figure 4.2: Scheme of ZnO's Synthesis Procedure.

4.3 Characterization Techniques

Several characterization techniques were used to analyze and draw conclusions about the sensor's properties. The chemical composition of the CF was studied, as well as its resistivity. After the ZnO growing process, a chemical and morphological characterization were also performed, in order to assess the structures deposited at TPU's substrate.

For a chemical and structural characterization, techniques such as Micro-Raman Spectroscopy and X-Ray Diffraction were performed, respectively. Differential Scanning Calorimetry (DSC) was used to evaluate the thermochemical propertiesof TPU. A morphological characterization using Scanning Electron Microscopy was also important to conclude about the ZnO growing. An electrical characterization was also performed in order to evaluate the Sheet Resistance of the electrodes used.

4.3.1 Micro-Raman Spectroscopy

Renishaw inVia Qontor micro-Raman spectrometer was used to take Raman measurements. Micro-Raman Spectroscopy was used to determine the substances present in the filafex filament and which one allows it to be conductive. For this reason, a 20 × 20 mm^2 3D

printed CF square was studied using a Horiba Jobin-Yvon HR800 spectrometer with a 532 nm laser. The power was 1%, which corresponds to 500 mV, and the exposure time was 45 seconds with 3 accumulations. This technique was also performed on a sample after the ZnO growth procedure to conclude about the effectiveness of this synthesis method.

4.3.2 X-Ray Diffraction

X-Ray Diffraction was also conducted on the CF sample to identify the conductive substance the filament was composed of. A TPU, a CF with transferred LIG, a TPU with transferred LIG and a carbon tape samples were also analyzed. The crystallinity of the resulting particles after the Zno growth procedure was also assessed by XRD. The analysis were performed between 10° and 90° (2 θ) with a scanning step size of 0.033° using a XRDynamic 500 from Anton Paar equipped with a PiXcel detector and a monochromatic Cu Kα radiation source with wavelength 1.540598 Å.

4.3.3 Sheet Resistance

The sheet resistance of the TPU and of all the materials used as electrodes was performed on a Biorad HL 5500 equipment at room temperature, with the aim of assessing their resistivity.

4.3.4 Differential Scanning Calorimetry

DSC was performed to analyze the behavior of TPU under elevated temperatures. This analysis aimed to determine the temperature range suitable for the ZnO synthesis processes. The equipment used was the DSC 204 F1 Phoenix, and the analysis was conducted over a temperature range of 20 °C to 540 °C.

4.3.5 Scanning Electron Microscopy

Scanning Electron Microscopy was an important technique to determine the presence of ZnO after the procedure used for its synthesis (described in 4.2.1). Before this technique was employed, samples were subjected to a 20 nm gold/palladium (80/20 wt%) coating. The equipment used was a Hitachi Regulus 8220 Scanning Electron Microscope (Mito, Japan) and it was performed at room temperature.

4.4 Evaluation of the Sensor's Response Under Different Impact Forces

The impact performance of a non-patterned design using carbon tape, CF, TPU with transferred LIG and CF with transferred LIG as electrode materials was evaluated using a homemade impact machine that applied forces between 30 N and 60 N with a frequency of 2 Hz. The voltage signal was measured using a 50 MHz bandwidth Digital Oscilloscope

(Tektronix, TDS 2001C). The resulting CSV files were analyzed using the feature "Quick Peaks" on OriginPro 2024. This feature finds peaks in data plots within a region of interest. All the positive and negative voltage peaks were registered and then peak-to-peak voltage was calculated. For each force, the mean and standard deviation were estimated based on 40 peak-to-peak voltages. The impact response of the different designs was also tested using CF as an electrode, as well as the impact response before and after the ZnO's growth. To assess the sensor's experimental detection limit, tests using weights from 200 g to 5 g were performed. FT and tremor emulated tests were also performed using the sensors' prototypes.

4.5 Final Prototypes

The sensor's final prototypes for the FT test and for the wristband to detect tremor were also modeled using SolidWorks and printed using UltiMaker S3 with TPU 95A. During the printing process, the bed temperature of the 3D printer was also kept at 0 °C and the extruder temperature was 225 °C. The infill used for all the prototype pieces was 15% and, for both active layers, the "Hexagon Holes" pattern was used.

In order to enable the ZnO growth (described in Section 4.2.1) on TPU's surface, an electrode that could be attached to the TPU sensor after that procedure was developed. If the electrode was later printed over the TPU substrate where the ZnO growth had already happened, some misprinting might have occurred. Hence, an attachment system was revealed to be a better option. The design of both prototypes was conceived in a way that allowed the attachment of the CF electrode (Figure 4.1e). Therefore, the active layer of both prototypes was increased to 3×2 cm^2.

The FT test is composed by 2 pieces; one for the thumb and one for the index finger. Considering the way that FT is tested, it was important to have an ergonomical design that could adapt to each patient's fingers. Different designs for the index finger were also developed and tested. The thumb piece, as well as the index finger pieces that were designed to cover the whole index finger, were printed vertically to the printing bed with a printing speed of 15 mm/s.

The wristband developed with the purpose of detecting tremor was printed laid down on the printer bed and the printing speed used was 25 mm/s.

FT tests took place and the procedure adopted was the same explained in 3.1, that consists in tapping the index finger to the thumb, while doing it with the highest amplitude and speed movement.

The wristband with the attached CF electrode was tested using the impact machine previously mentioned, where the force exerted was controlled. Moreover, it was also tested for emulated tremor.

5

Results and Discussion

In this chapter, the results obtained will be discussed and analyzed. In particular, the results of the morphological, structural and chemical analyzes of the materials incorporated in the sensors will be presented. Additionally, studies regarding the electrical properties of the materials used as electrodes and the response of the developed sensors under different impact forces (30 N to 60 N) will be analyzed. The insights obtained from these analyzes will contribute to a deeper understanding of the materials used and their potential applications in the area of triboelectric and piezoelectric pressure sensors.

5.1 Electrode Materials

The materials tested as electrodes, namely carbon and LIG, were studied using Raman Spectroscopy and X-Ray Diffraction. Additionally, their electrical properties were evaluated based on Sheet Resistance studies. Each material was used as an electrode and the electrical response of sensors with different electrode types was studied for impact forces between 30 N and 60 N (with a 2 Hz frequency impact).

5.1.1 Raman Spectroscopy

The Raman spectrum of TPU was analyzed and compared with the ones in the literature.

MRS reports the frequency shifts as a function of excitation photon energy and is based on the scattering effect. When a laser irradiates the sample, photons will interact with it and produce new scattered photons. Raman spectroscopy measures the shift of the inelastic scattered photon after this interaction. This technique produces a Raman spectrum consisting of peaks or bands, with their positions determined by the vibrational frequencies of the molecules in the sample. By analyzing these frequencies, it becomes possible to identify the specific chemical compounds present in the material [87, 88].

When analyzing the spectrum of TPU, presented in Figure 5.1, the typical TPU peaks can be observed [89–91]. The Raman shifts of the most intense peaks for TPU are reported to be around 866, 1185, 1617, 2875 and 2926 cm^{-1}. These peaks match the ones observed in the figure, although the last two are less closely aligned. The peak at 1617 cm^{-1} is related

to the aromatic structure stretching and the last two peaks correspond to C-H stretching vibrations [92].

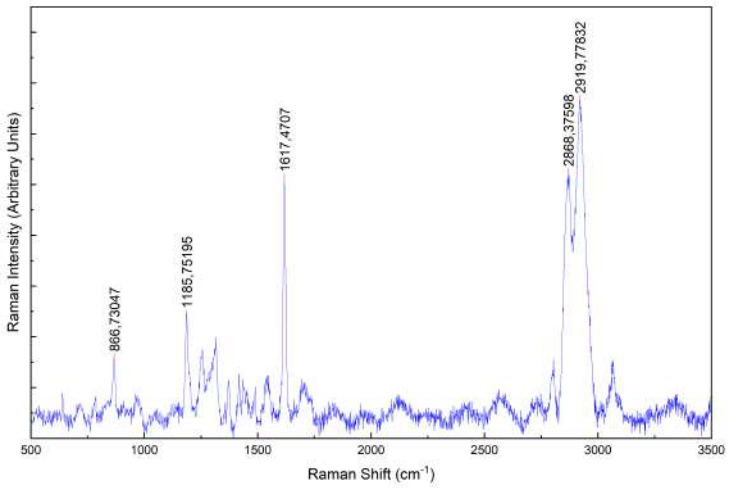

Figure 5.1: Raman Spectrum of TPU.

Raman Spectrum of CF was also analyzed, as it is a commercial material whose composition is not detailed. The sample was analyzed in three different areas and Figure 5.2 shows a representative spectrum of the CF filament.

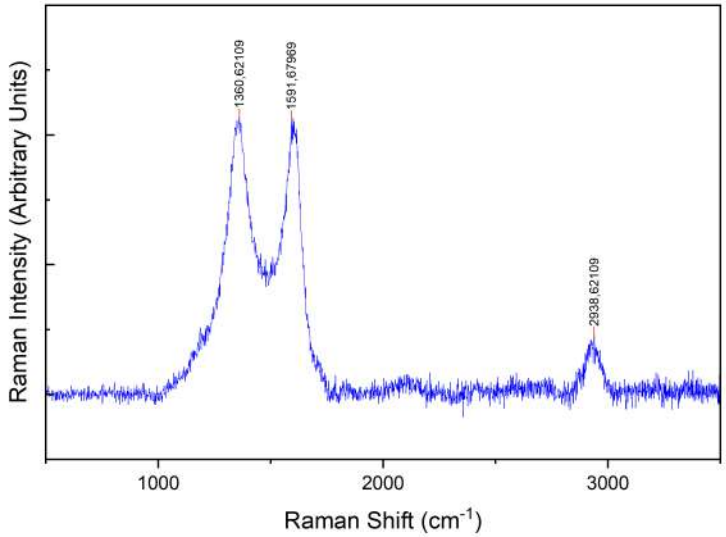

Figure 5.2: Raman Spectrum of Conductive Filaflex.

The Raman spectra of carbon-based materials usually show different peaks. Two peaks are commonly detected, called the D peak and the G Peak. The D Peak concerns sp^2 hybridized carbon structures and is related to the disorder of the carbon material. It is the

result of dislocations in the lattice [93, 94]. The G Peak is associated with the vibration of carbon bonds and indicates the presence of sp^2 carbon, regardless of the order or disorder of the material [94]. The 2D Peak is also commonly present in carbon-based materials [95].

By observing the Raman graphics, it is possible to detect three peaks: the first one, corresponding to the D Peak, around 1360 cm^{-1}, the second one, the G Peak, around 1590 cm^{-1} and the third peak is located around 2938 cm^{-1}.

According to Dychalska *et al.* [93] a D-Band with a Raman shift of 1345 cm^{-1} and a G-Band between 1500 and 1600 cm^{-1}, as it is shown in Figure 5.3, corresponds to amorphous carbon.

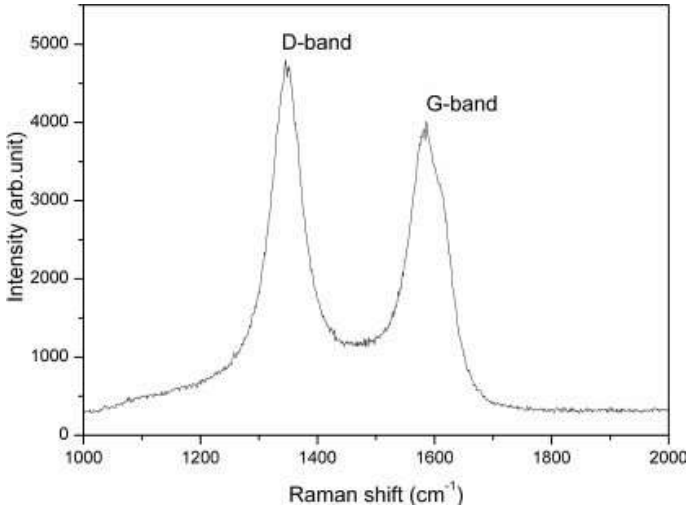

Figure 5.3: Raman Spectrum of Amorphous Carbon. Adapted from Dychalska (2015) *et al.* [93].

The third peak visualized, at 2938 cm^{-1}, could correspond to the highest Raman peak of TPU that was previously detected (Figure 5.1) and it was reported of being around 2926 cm^{-1} [91]. Comparing the obtained peaks with the ones reported in literature, it was concluded that amorphous carbon is present in the composition of CF . X-Ray Diffraction was also performed to characterize this material.

5.1.2 X-Ray Diffraction

X-Ray Diffraction was also performed to identify the conductive material present in the CF filament. This technique is specifically used to study crystalline structures. When a beam of X-rays is directed at a material, it is scattered by the atomic layers or crystalline planes, resulting in the phenomenon of diffraction. A detector that rotates at an angle of 2θ records and processes the diffracted X-rays and their intensity is registered as the angle varies [96, 97].

If the sample is crystalline, the atoms are arranged in a regular, well-defined structure with distinct planes. However, if the material is non-crystalline, the scattered X-rays do

not interfere constructively and, consequently, no distinct diffraction peaks are formed [97].

By analyzing Figure 5.4, which displays the XRD patterns of CF, CF with transferred LIG, TPU with transferred LIG, and TPU, a correlation between the diffraction peaks and the materials can be observed.

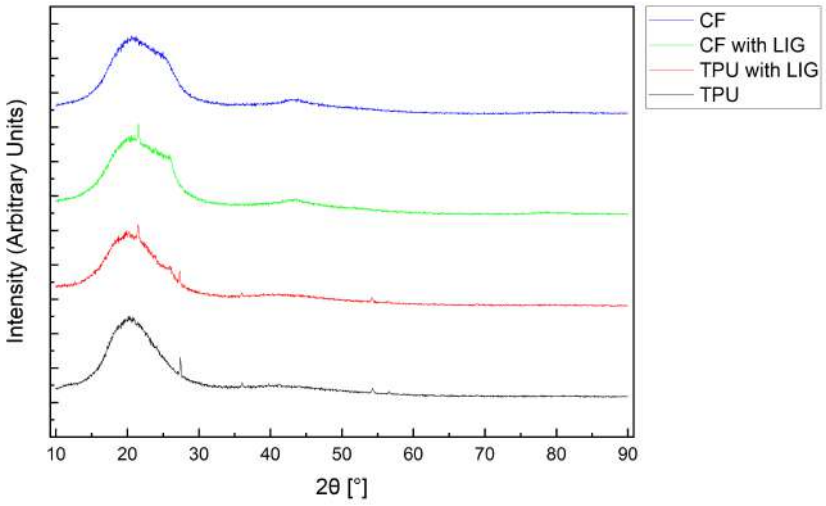

Figure 5.4: XRD Patterns of CF, CF with transferred LIG, TPU with Transferred LIG and TPU.

A large band between 15° and 25° is present in all spectra, suggesting that this peak is associated with the polyurethane material [98]. The TPU and TPU with transferred LIG have a common peak, around 27°, that may be related to the thermoplastic polyurethane material.

Regarding the CF electrode, no sharp peak is observed. Instead, two broad bands appear: one between 15° and 30 ° and another between 40° and 47°. These bands are also present for the CF with transferred LIG electrode, indicating that they regard compounds of the conductive filaflex filament.

For the electrodes with transferred LIG (CF with transferred LIG and TPU with transferred LIG), a distinct peak near 22° is detected. Considering that this peak is unique to these electrodes, it may be attributed to the presence of LIG. Additionally, a similar peak around this value has been reported in previous research [99, 100], supporting the hypothesis that the obtained peak is related to the LIG.

In the case of amorphous carbon, where the atoms are distributed randomly, there is no constructive interference between the scattered X-rays, which leads to no diffraction peaks being formed [97].

Considering these XRD results, and those previously obtained from Raman spectroscopy, it was concluded that CF predominantly contains amorphous carbon.

5.1.3 Sheet Resistance

Sheet Resistance measurements were performed to assess the electrical properties of all the electrodes used.

Sheet Resistance values of TPU, carbon tape, CF, CF with transferred LIG and TPU with transferred LIG were acquired. However, the samples tested did not have the same thickness; hence, resistivity was calculated using the following equation,

$$\rho_s = \frac{\rho}{t} \tag{5.1}$$

where ρ_s, ρ and t represent the sheet resistance, resistivity and thickness, respectively.

Table 5.1 shows the mean resistivity ± SD. Materials are ordered from the highest resistivity to the lowest.

Table 5.1: Results of Sheet Resistance For TPU, Carbon Tape, CF, CF with Transferred LIG and TPU with Transferred LIG.

Material	$\overline{\rho}$ **± SD** (Ω/**cm**)
TPU	$4 \times 10^{10} \pm 2 \times 10^{10}$
Carbon Tape	$3 \times 10^{3} \pm 4 \times 10^{1}$
Conductive Filaflex	$9 \times 10^{1} \pm 1 \times 10^{2}$
Conductive Filaflex With LIG	$9 \times 10^{1} \pm 7 \times 10^{-4}$
TPU With LIG	$3 \times 10^{-1} \pm 6 \times 10^{-4}$

TPU presents the highest resistivity, as expected, since polymers have low conductivity and therefore high resistivity. Although TPU has a higher resistivity than CF, TPU with transferred LIG shows the lowest resistivity, but its value is still in the same order of magnitude as CF with LIG. CF has a resistivity value nearly ten times higher than the one registered for CF with LIG, while for TPU this value is 10^{11} higher than the one registered for TPU with transferred LIG.

Later, the impact response using these materials as electrodes was studied.

5.1.4 Impact Performance

The impact response of the "Square Design" (Table 4.1), a non-patterned design that worked as the active layer, was tested using all the conductive electrodes mentioned earlier (carbon tape, CF, TPU with LIG and CF with LIG) with the aim of selecting the best one for the sensor.

Figure 5.5 shows the peak-to-peak average voltage generated by the impact between the TPU and the different electrodes, under impact forces of 30 N, 40 N, 50N and 60 N, which translates to a pressure of 75 kPa, 100 kPa, 125 kPa and 150 kPa.

Carbon tape was firstly tested to understand if the use of carbon materials as electrodes of sensors where TPU was used as an active layer was effective. In the context of the triboelectric series, when two materials come into contact and then separate, one material

tends to lose electrons and become positively charged, while the other tends to gain electrons and become negatively charged, generating a potential difference [23]. As carbon is expected to be more positively charged than TPU, it may have a tendency for losing charges, becoming positively charged when contact between the two happens. These charges will be transferred to TPU, which will become negatively charged. When the external force ceases and the two materials are separated, an output voltage can be detected and measured using an oscilloscope.

By analyzing Figure 5.5, a common observation across all electrodes is the effect of increased pressure. For each material, a higher impact results in a higher output voltage. This is expected because greater pressure can increase the contact area or the deformation between the materials, leading to the exchange of a larger number of charges. Nevertheless, the increase in voltage with pressure will not continue indefinitely, as there is a limit to the number of charges that can be generated or stored by the materials due to their physical and chemical properties, and once a threshold pressure is reached, further increases in pressure will not result in a higher output voltage, as the system reaches charge saturation. Graphically, this charge saturation is converted into a plateau.

As can be seen in Figure 5.5 and table in Appendix A, for all the pressures, the CF electrode lead to the highest OV, while carbon tape lead to the lowest one. TPU with LIG and CF with LIG reveal a moderate OV.

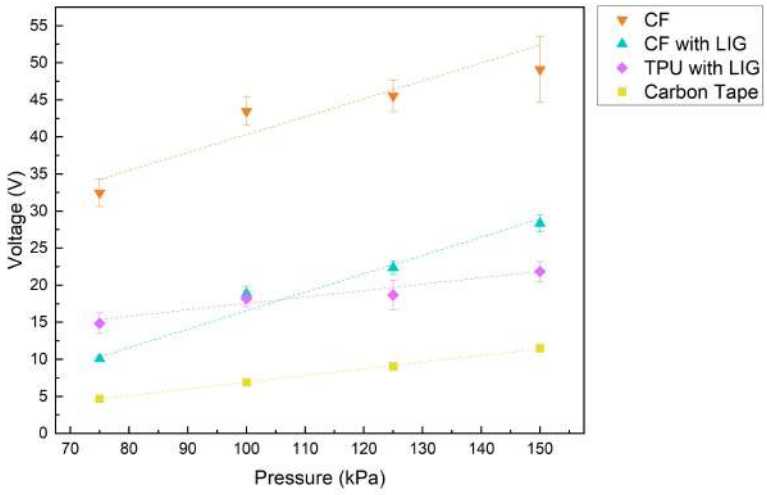

Figure 5.5: Peak-to-Peak Voltage of Different Electrodes Combined with the Square Design Upon Impact Forces of 30 N, 40 N, 50 N and 60 N.

The relatively small error bars suggest a consistency of the measurements. Furthermore, the standard deviations of each electrode have the same order of magnitude. All of this leads to the conclusion that results are precise and the sensors present a stable and reproducible response.

Regarding the sensitivity of the sensor with each electrode, the slope of each linear regression was studied. The ratio between variations in the output signal and the input

variable in a sensor results in its sensitivity [101]. The slope indicates the rate at which voltage increases and the obtained results are shown in Table 5.2. CF with LIG electrode shows the highest slope and, therefore, the highest increase in voltage with pressure, while TPU with LIG electrode shows the lowest slope and slowest increase in voltage with pressure, even though these were not the electrodes that recorded the highest and the lowest voltage overall.

Although there is some importance in using an electrode that provides high OV (so that the finger-tapping signal can easily be distinguished from noise), the chosen electrode should be the one that, more than showing the highest OV, can maintain its integrity over the impact and yield sensors with high sensitivity.

Table 5.2: Sensitivity of Sensors Composed of a Non-patterned Active Layer and CF, CF with LIG, TPU with LIG and Carbon Tape as Electrodes.

Electrode	**Sensitivity (V/kPa)**
CF	0.24 ± 0.07
CF with LIG	0.25 ± 0.02
TPU with LIG	0.09 ± 0.01
Carbon Tape	0.090 ± 0.001

Regarding electrode's integrity, it is worth mentioning that the electrodes with transferred LIG presented cracks after 200 impact cycles. Moreover, the LIG started detaching from the substrate, resulting in an active layer with LIG, as can be seen in Figure 5.6.

(a) TPU Substrate. (b) CF With Tranferred LIG. (c) TPU With Tranferred LIG.

Figure 5.6: Resultant Samples after Impact Tests with the Presence of LIG (the depicted scale is of 750 μm).

According to the presented results, the CF electrode was the one used to develop the FT sensor.

5.2 Sensor Fabrication

The sensor was entirely fabricated using 3D-printed TPU. In this sub-chapter, conclusions regarding the 3D printing process will be presented.

(DSC) was employed to analyze the thermal behavior of TPU, providing insights into its performance at elevated temperatures.

The effectiveness of the ZnO deposition process on the surface of TPU samples will be evaluated through techniques such as XRD and SEM.

Finally, impact response tests were conducted to investigate the influence of different designs, contact areas, and the presence of ZnO on the output voltage. Impact tests were also performed to assess the sensor's detection limits.

5.2.1 3D-Printing

The 3D-printing process started with an investigation into the different adjustable parameters, including infill, infill pattern and printing speed. All these parameters were adapted for each design shown in Table 4.1 according to what led to the best samples' features.

The protruding designs, such as the Cones, Spheres, Waves and Hexagons were the ones whose height and distance between each detail influenced the final piece. In these cases, a 1.5 mm height and a 2 mm distance between each little design (for instance, between each cone) revealed to be the minimum values that could be used and produce a good quality piece after being printed. The printing speed directly impacts its final condition. These pieces, having such small details, required a low printing speed. The Archimedean designs revealed an easier printing process, where a higher printing speed was used and the width and distance between each protruding was lower (1 and 0.5 mm, respectively). Smooth designs' printing speed was increased to 35 mm/s, since a higher speed did not jeopardize its final quality. The square designs were all 20×20 mm^2 and the circles had a diameter of 22.6 mm, so that all the designs had an area of 4 cm^2.

Later, the active layer had to be extended in order to add space for the electrode to be attached after the ZnO growth. The FT prototype was composed of three 3D-printed pieces: the thumb (Figure 5.7), the index (Figure 5.8) and the electrode (Figure 4.1e). The thumb piece prototype had a diameter of 2 cm, with a printed-in rectangle with "Hexagon Holes" design (the active layer). Different index finger designs were developed with the aim of identifying the most viable one in terms of comfort and OV generated. This piece, as well as the index one, showed its comfort, lightness and ergonomic design during FT tests. It is worth noting that this prototype could be resized and adapted to the finger size of each patient.

A 20 cm size wristband sensor was also developed (Figure 5.9) to detect tremor. This prototype has an active layer with the same size and design as the FT sensor prototype, as well as a design that could attach the CF electrode. Besides the attachment for the electrode, another one was designed so that the same wristband could fit a diverse number of patients, with each person being able to choose the hole to attach, according to their wrist size.

Regarding the 3D-printed process, it is generally possible to conclude that an infill of 15% while maintaining a printing speed equal to or below 25 mm/s with deactivated "enable retraction" feature would yield a final piece with the desired characteristics, such as good flexibility and detail. Deactivating the retraction was a crucial step because, being

(a) Sensor With Attached Electrode.

(b) Sensor Prototype.

(c) Active Layer.

Figure 5.7: Prototype Sensor for FT Test.

(a) Ring Finger Design.

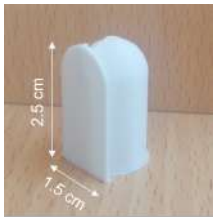

(b) Finger with plane.

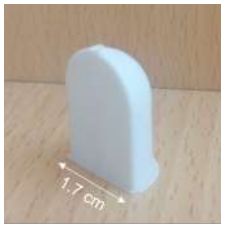

(c) Flat Finger.

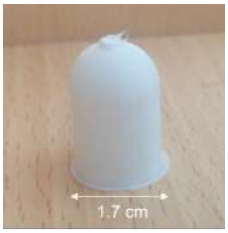

(d) TPU Finger.

Figure 5.8: Index Finger Designs.

(a) Wristband.

(b) Wristband with Attached Electrode.

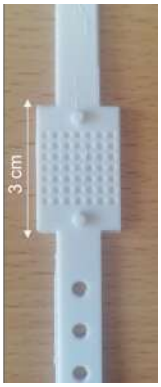

(c) Active Layer.

(d) Wristband Attachment.

Figure 5.9: Wristband Design.

TPU a thermoplastic material, it tends to stretch out when the extruder pulls the filament, which can cause an inconsistent extrusion and even clogging. In short, this feature enables a smoother and more continuous extrusion, leading to fewer printing flaws.

5.2.2 Impact Response of Different Active Layers

The impact performance of sensors composed of an electrode of CF and active layers of TPU with different patterns (Table 4.1) was tested to evaluate how the designs affected the OV. The material used for the electrode was CF because, especially in contact with sharp

protrusions like "Cones", it was the one that would maintain its integrity, contributing to the decrease of variability. All the designs tested had an active area of 4 cm^2 and a 2 mm thickness. Tests were performed for 30 N, 40 N, 50 N and 60 N and the results can be observed in Figure 5.10 and Table C.1 in Appendix C.

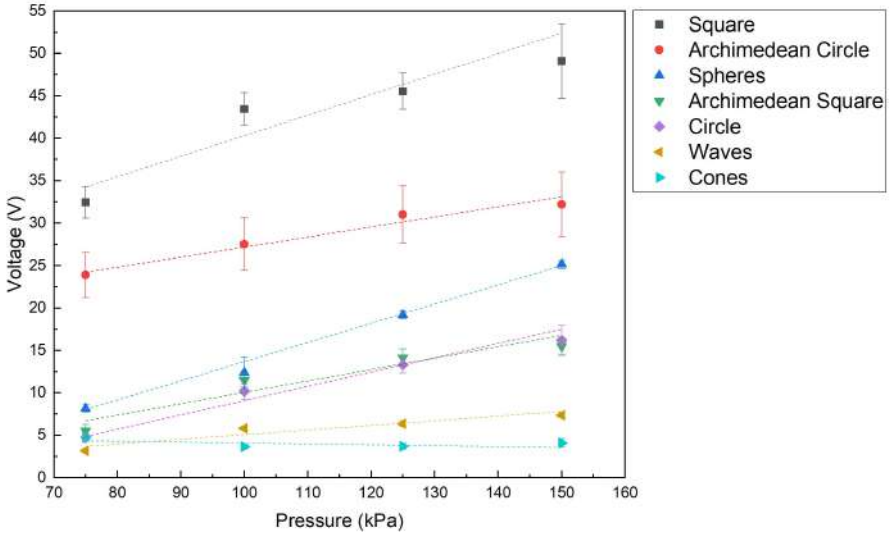

Figure 5.10: Impact Tests for Different Designs Upon Impact Forces of 30 N, 40 N, 50 N and 60 N Using the CF Electrode.

For each design and pressure impact, 40 peaks were analyzed and mean and standard deviation were calculated. The slopes depicted on Figure 5.10 represent the sensor's sensitivity for each active layer pattern. Table 5.3 shows the sensitivity values of the sensors tested. Designs with bigger protrusions, like "Cones" and "Waves", registered the lowest output values, probably due to the size of the protrusions. Since it is not possible to print these designs with reduced heights due to the inherent limitations of the printer, the overly large dimensions of the protrusions may lead to a decrease in the contact area, resulting in a lower output voltage. For this reason, and also because it would not create the best surface for the electrode to be attached, the use of these designs in the final prototype was discarded.

The "Square" design showed the highest output response for all the pressures applied, followed by the "Archimedean Circle" and "Spheres". The "Archimedean Square" and "Circle" designs revealed a very similar OV. Since both share the same active layer area and 3D-printing parameters, a comparable output voltage was expected. Therefore, the results obtained are well-aligned with theoretical predictions.

Table 5.3: Sensitivity of the Sensors for Different Active Layer Patterns Using the CF Electrode.

Pattern	Sensitivity (V/kPa)
Square	0.24 ± 0.07
Archimedean Circle	0.12 ± 0.02
Spheres	0.23 ± 0.01
Archimedean Square	0.13 ± 0.03
Circle	0.17 ± 0.02
Waves	0.05 ± 0.01
Cones	-0.011 ± 0.009

5.2.3 Differential Scanning Calorimetry

DSC was applied to the polymer to study its thermal stability. This technique determines the temperature and heat flow that induce material transitions as a function of time and temperature. DSC measures the heat flow difference between a sample and a reference while both are under a controlled temperature. The thermal power needed to keep both at the same temperature is measured and plotted as a function of temperature [102]. Figure 5.11 represents the DSC for TPU.

By analyzing the weight loss curve of the graph (green curve), it is possible to conclude that until 550 °C is reached, 86.28% of the sample's weight was lost.

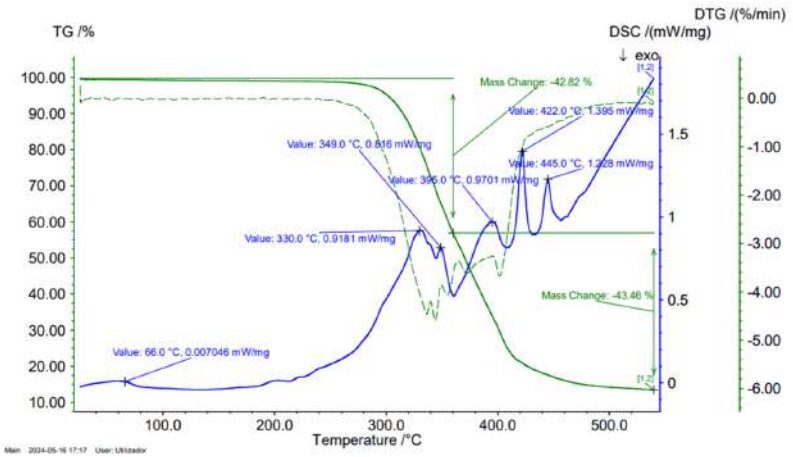

Figure 5.11: Differential Scanning Calorimetry of TPU.

The DSC curve (blue curve) reveals endothermic peaks at 66 °C, 330 °C, 349 °C, 395 °C, 422 °C and 445 °C. The first peak can be related to heat absorption, indicating the beginning of TPU's melting [103]. Peaks between 330 °C and 340 °C may correspond to urethane bonds decomposition, whereas peaks at 422 °C and 445 °C suggest the polyetherol degradation process [104]. The final peak, localized at a higher temperature, corresponds to an advanced decomposition of the polymer, possibly related to carbon bonds (C-C) breaking [104].

In conclusion, until 300 °C is reached, TPU shows good thermal stability. Above this temperature, there is a significant mass loss, indicating degradation of the polymer.

Taking into account these results, it was demonstrated that the substrates did not undergo significant changes at the synthesis temperatures used. This ensures the structural integrity of the materials throughout the process, indicating that the applied thermal conditions are suitable for preserving the desired properties of the substrates without compromising their stability.

5.2.4 ZnO Growth

Based on the procedure established by Kumbhakar *et al.* [73], the growth of ZnO structures on TPU substrates was performed at 60 °C and 70 °C.

Considering DSC results, the thermal bath temperature for the ZnO growth was kept at 60 °C, as reported by Kumbhakar *et al.* [73]. The upper limit of the synthesis temperature was 78 °C, as it is the ebullition point for ethanol, one of the solvents used for the solution that will lead to the ZnO growth. Therefore, 70 °C was the chosen temperature, since it did not seem to cause major changes in TPU and allowed a 3-hour ZnO synthesis without the complete evaporation of the solvents. This way, the influence of temperature on the growth and morphology of ZnO structures was studied.

The structures and morphology of the particles grown at the surface of the TPU substrates were analyzed using XRD and SEM. XRD was used to study the crystal structures formed after the ZnO's growing procedure and SEM was performed to assess their morphology.

5.2.4.1 Scanning Electron Microscopy

SEM analysis took place to study the morphology of the Zinc-based structures that grew on the surface of the TPU substrates. This technique uses an electron beam and once it reaches the sample's surface, the beam is scattered. The signals resulting from the interaction between the electrons and the sample are detected and converted into an image that represents the sample's morphology and composition [105]. It is necessary to have a conductive sample in order to avoid charge accumulation on its surface and capture good-quality images. As TPU is a polymer, it was necessary to previously subject the samples to a thin film conductive coating of gold/palladium.

The images obtained are shown in Figure 5.12, which correspond to samples that were kept at 60 °C during the ZnO's growing procedure. Figure 5.13, presents the images of the samples resulting from the growth process performed at 70 °C.

In image A of each Figure (5.12 and 5.13), the presence of thin nanosheets on the surface of the TPU substrate is clearly visible. It is observed that the hexagonal holes provided a more favorable site for deposition when compared to the smooth areas of the sample.

Figure 5.12 illustrates images with thin and elongated structures that are consistent with the morphology of nanosheets. These images have been compared with those documented in the literature for ZnO nanosheets. Images C and D of Figure 5.12, when compared to images reported by Wang *et al.* [106] after a two-step growth process, suggest the presence of ZnO nanosheets. Image D exhibits similarities to images of mesoporous nanosheets, where $Zn_5(OH)_8Cl_2$ hexagonal nanosheets were converted thermally, as documented by Zhu *et al.* [107]. Liang *et al.* [108] also reported similar images for pristine porous ZnO nanosheets.

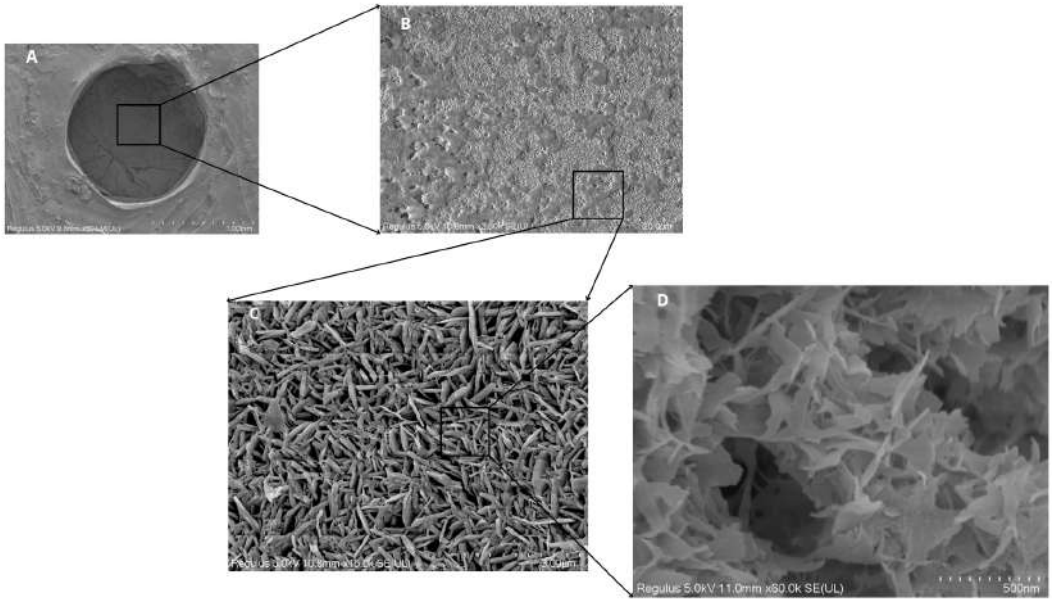

Figure 5.12: SEM Images of "Hexagon Holes" Sample Resulting from the Growth Process Performed at 60 °C. (A) 50× Magnification, (B) 2.5× Magnification, (C) 15× Magnification, (D) 60× Magnification.

Concerning the sample maintained at 70 °C (Figure 5.13), slight differences in the shape of the structures grown on the surface of the polymer sample were observed. Images C and D suggest the presence of some ZnO nanoflowers [109, 110] or nanoplates [111, 112], when compared with the literature. Therefore, the increase in temperature appears to have influenced the morphology of the deposited structures.

The procedure for the ZnO growth was also tested using the "Hexagons" pattern. The surface of the TPU substrates after the synthesis was studied using SEM and the results are presented in Appendix B. Comparing the designs, it was concluded that holes facilitate ZnO growth, as it allows for better ZnO deposition. For this reason, the "Hexagons Holes" design was chosen for the final prototype. SEM was also used to investigate samples with a synthesis time of less than 3 hours (Appendix B). However, a decrease in synthesis time may cause a reduction in the quantity of Zinc-structures deposited, as well as originate different morphologies.

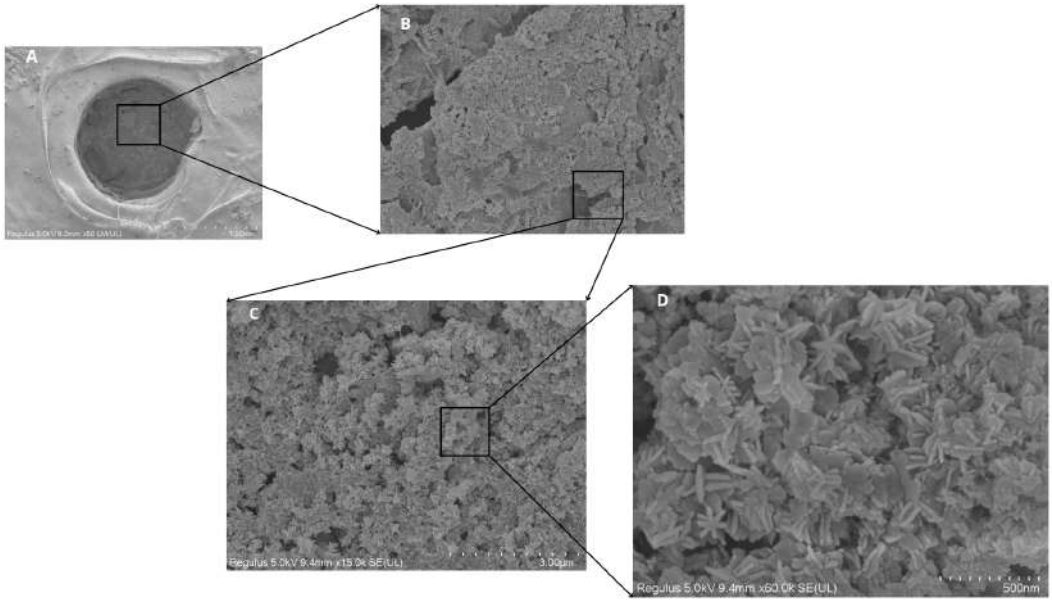

Figure 5.13: SEM Images of "Hexagon Holes" Sample Resulting from the Growth Process Performed at 70 °C. (A) 50× Magnification, (B) 2.5× Magnification, (C) 15× Magnification, (D) 60× Magnification.

5.2.4.2 X-Ray Diffraction

XRD was performed to conclude about the presence of ZnO. $Zn(OH)_2$ is a precursor substance in ZnO's hydrothermal synthesis, which, upon precipitation, strongly tends to be transformed into ZnO [113]. Thus, the presence of $Zn(OH)_2$ was also evaluated. The International Centre for Diffraction Data (ICDD) datasheet for both materials was analyzed and its characteristic peaks were compared with those observed in the XRD pattern.

Figure 5.14 and Figure 5.15 show the XRD patterns for TPU and TPU after the ZnO synthesis process, as well as ZnO's and $Zn(OH)_2$ ICDD patterns. Figures 5.14a and 5.15a refer to the sample resulting from the growth process performed at 60 °C, while 5.14b and 5.15b refer to the one performed at 70 °C.

By analyzing Figure 5.14, it was concluded that the diffraction pattern of the TPU shows a broad band around 20°, which is present in the diffractograms of the samples both before and after synthesis. Both samples exhibit a peak at 36°, which is observed in the diffractogram of the sample before and after the ZnO synthesis process, leading to the conclusion that this peak is caused by a component of the TPU filament. Additionally, both samples show a small peak around 69°, which may correspond to ZnO's characteristic peak at 69.1°. Regarding the second graph (5.14b), a peak at 56.58° coincides with ZnO's characteristic peak reported at 56.60°. All other visible peaks not previously mentioned are likely associated with the TPU material rather than ZnO.

Therefore, since the sample subjected to the highest temperature shows a greater

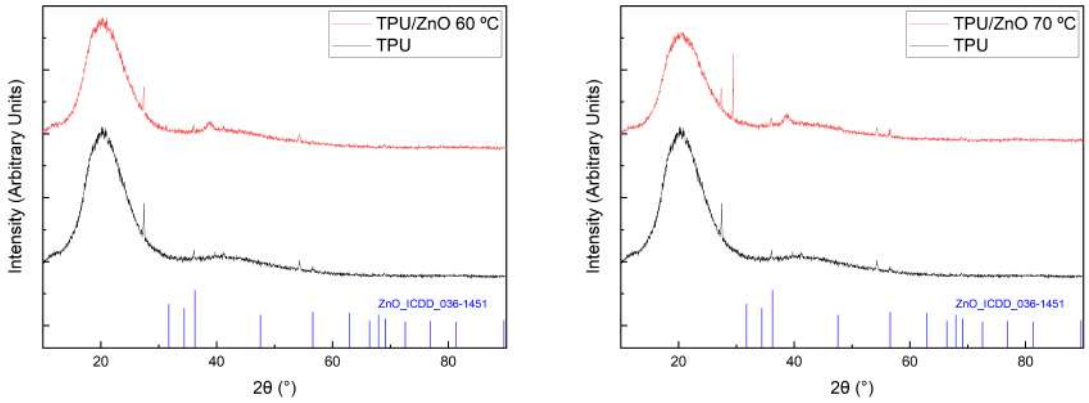

(a) Temperature of Synthesis: 60 °C. (b) Temperature of Synthesis: 70 °C.

Figure 5.14: X-Ray Diffraction Spectra for Samples Subjected to ZnO Growing Process at 60 °C (a) and 70 °C (b) Compared with ZnO's ICDD Datasheet.

number of peaks matching those reported for ZnO, it is concluded that an increase in temperature may have favored the synthesis of ZnO. According to the ICDD pattern of $Zn(OH)_2$, the most intense peaks can be found at 20.1°, 20.8°, 25°, 27.1°, 27.7°, and 40.6°.

In both conditions studied (Figure 5.15), two peaks around 20° and 27.4° are observed. However, these peaks are also present in the spectra of thermoplastic TPU, suggesting that they may be related to TPU rather than $Zn(OH)_2$. Alternatively, the TPU peaks may be masking those of $Zn(OH)_2$.

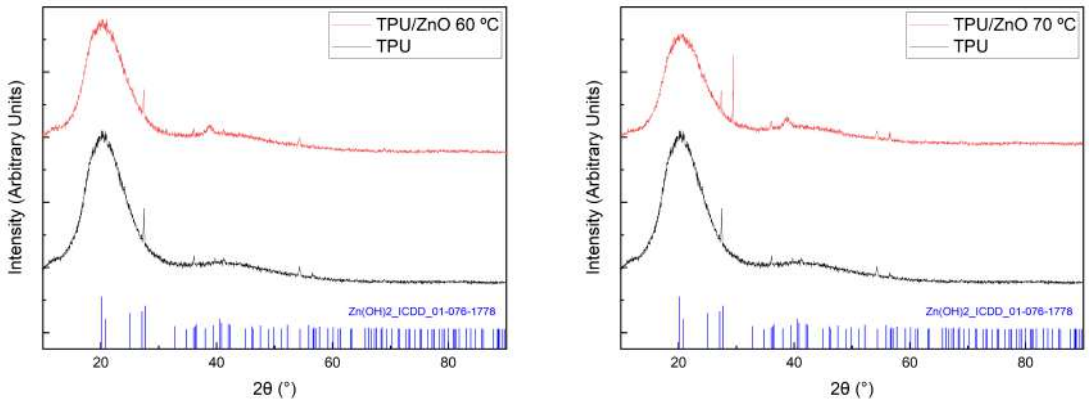

(a) Temperature of Synthesis: 60 °C. (b) Temperature of Synthesis: 70 °C.

Figure 5.15: X-Ray Diffraction Spectra for Samples Subjected to ZnO Growing Process at 60 °C (a) and 70 °C (b) Compared with $Zn(OH)_2$'s ICDD Datasheet.

Furthermore, in both conditions, a peak appears around 38°, which is not evident in the TPU pattern. $Zn(OH)_2$ has a characteristic peak at 40.6°; however, given the deviation of 2.6°, the peak around 38° may not be caused by $Zn(OH)_2$ but rather by other present substances. Therefore, the hypothesis of $Zn(OH)_2$ being synthesized during the process described at 4.2.1 was not disregarded.

Raman spectroscopy was subsequently performed to confirm the chemical synthesis of ZnO.

5.2.4.3 Raman Spectroscopy

As the XRD results were inconclusive, with characteristic peaks of the substance overlapping those of TPU, micro-Raman spectroscopy was conducted to confirm the presence of ZnO. The analysis focused on the range where the characteristic peaks of ZnO are typically located. The Raman spectra of TPU and TPU after undergoing the ZnO synthesis procedure are presented in Figure 5.16. Peaks around 99, 331, 384, and 438 cm^{-1} were observed in the spectrum of the treated sample but were absent in the spectrum of pristine TPU. These peaks were subsequently compared to the characteristic peaks of ZnO. According to the literature, peaks at 98 and 437 cm^{-1} are related the ZnO nonpolar optical phonons and a second order peak is assigned at 328 cm^{-1} [114]. A peak at 385 cm^{-1} is also a characteristic ZnO peak [114]. Therefore, it was possible to confirm the successful incorporation of ZnO into the TPU substrates following the synthesis procedure.

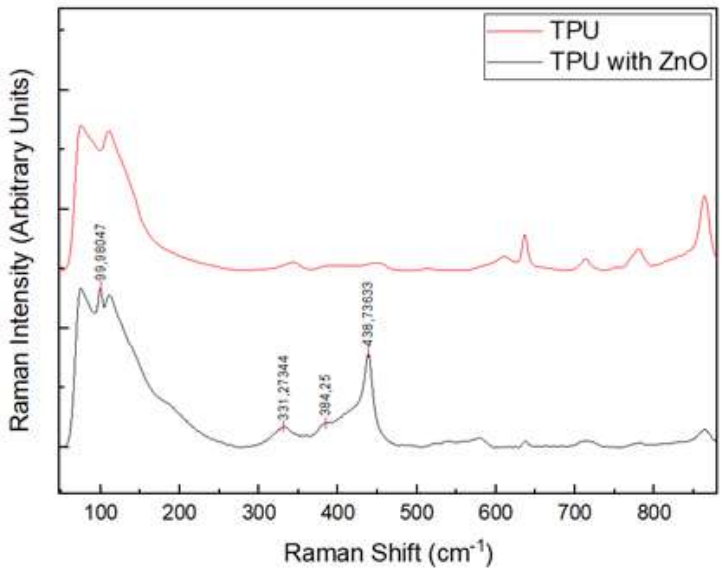

Figure 5.16: MRS of TPU before and after undergoing the ZnO growth process.

5.2.4.4 Final Prototypes

The following results regard the impact tests performed using the final prototypes.

Although the "Square" design showed the highest OV, the "Hexagon Holes" design was used for the active layer of the final prototypes, as it is expected to promote ZnO's depositions. The active layer was increased by 2 cm^2 relative to the active layers used on previous tests, so that the CF electrode (Figure 4.1e) could be attached.

Samples with the "Hexagon Holes" design were tested with and without the ZnO growing process. In this case, samples were tested with the electrode attached and the

TPU layer used had a 6 cm^2 surface and also had 2 mm of thickness. Like the previous impact response tests, the impact forces used were 30 N, 40 N, 50 N and 60 N, and the results can be seen in Figure 5.17 and Table 5.4. The resultant output signal for each sample and force can be observed in Appendix D.

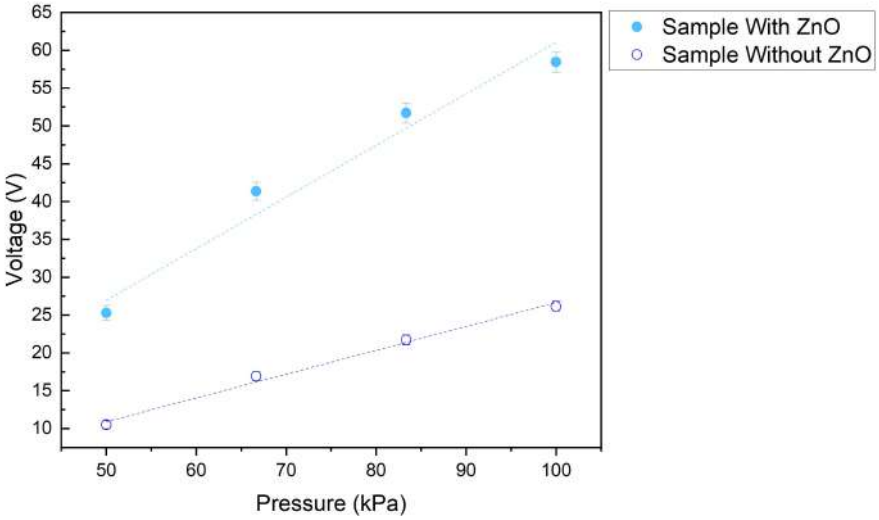

Figure 5.17: Impact Tests for Prototypes with an Active Layer of "Hexagon Holes" With and Without ZnO Upon Impact Forces of 30 N, 40 N, 50 N and 60 N.

Table 5.4: Results of Peak-to-Peak Voltage for Prototypes With and Without ZnO.

	Sample with ZnO		**Sample without ZnO**	
Pressure (kPa)	**Peak-to-Peak Voltage ± SD (V)**	**Sensitivity (V/kPa)**	**Peak-to-Peak Voltage ± SD (V)**	**Sensitivity (V/kPa)**
50	25 ± 1	0.68 ± 0.1	10.5 ± 0.5	0.31 ± 0.02
67	41 ± 1		16.9 ± 0.6	
83	52 ± 1		21.7 ± 0.7	
100	58 ± 2		26.2 ± 0.6	

The influence of ZnO on the OV was pronounced, as it was observed that across all tested pressure levels, the presence of ZnO resulted in more than a twofold increase in the OV. This substantial enhancement underscores the significant role of ZnO in boosting the electrical response.

The standard deviation associated with the peak-to-peak voltage computed for each impact force is small, which indicated the sensors produced present a stable response and high reproducibility.

The linear regression slope, i.e., the sensor's sensitivity, increased twofold in the presence of ZnO, indicating that, under identical pressure impacts, a sensor containing ZnO produces an output voltage that is twice as high as that generated by a sensor lacking this substance.

The successful growth of ZnO on the sensor substrate has been demonstrated, showing that ZnO effectively enhances the OV of the sensor. This improvement is significant, as

it adds substantial value to the development of the finger-tapping sensor being pursued, as the sensor is able to discriminate among close impact force values, due to its high sensitivity.

In order to test the limit detection of the developed prototype, weights of 200 g, 100 g, 50 g, 20 g, 10 g and 5 g were positioned on top of the attached CF electrode with TPU substrate. Results are presented in Figure 5.18 and Table 5.5.

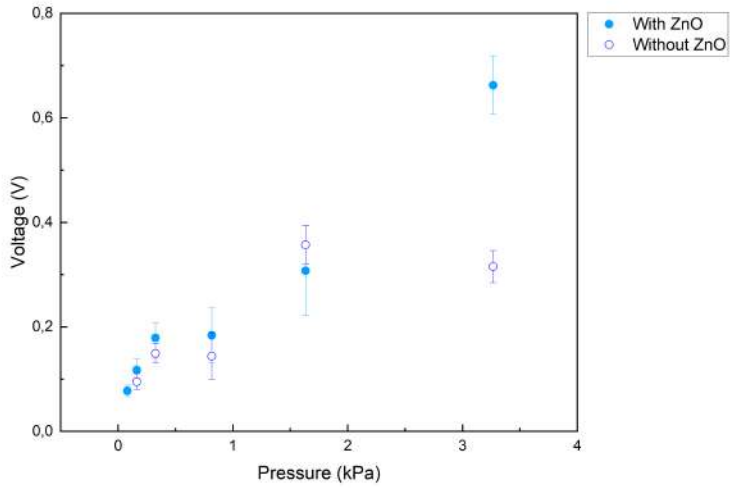

Figure 5.18: Impact Tests to Identify Limit Detection in Prototypes With and Without ZnO.

Table 5.5: Results of Peak-to-Peak Voltage for Limit Detection.

	Peak-to-Peak Voltage ± SD (V)	
Pressure (kPa)	**Sample With ZnO**	**Sample Without ZnO**
3.27	0.66 ± 0.06	0.32 ± 0.03
1.63	0.31 ± 0.09	0.36 ± 0.04
0.82	0.18 ± 0.05	0.14 ± 0.04
0.33	0.18 ± 0.03	0.15 ± 0.02
0.16	0.12 ± 0.02	0.10 ± 0.02
0.08	0.08 ± 0.01	-

As it was expected, for the sample with ZnO, the higher the weight used, the higher the pressure exerted and, consequently, a higher OV was generated. However, regarding the sample without ZnO, there is a fluctuation in OV between 3.27 kPa and 1.63 kPa and between 0.82 kPa and 0.33 kPa, where the lower pressure value registered the higher OV.

For ZnO treated substrate it was possible to identify peaks generated by the 5 g weight, while for the TPU without ZnO it was not possible to distinguish with accuracy peaks created by the impact of the weight.

The 100 g weight generated a higher OV for the sample without ZnO when compared with the one with ZnO. This outcome and the fluctuations registered for the sample without ZnO were unexpected and contradict the initial hypothesis. However, it may be attributed to errors in peak identification or variations in the drop height. Although all

weights were intended to be dropped from a height of 4 cm from the tested sample, slight variations in height could have introduced discrepancies, leading to these results.

These impact tests led to the conclusion that the developed sensor has a detection limit of 0.08 kPa.

Finger-tapping tests were conducted using the prototype for FT depicted in Figure 5.7. Various designs for the index finger (Figure 5.8) were also evaluated to assess the influence of the contact area during impact and to determine the comfort level of each design. These designs and the movement tested can be seen in Figure 5.19. Figure 5.20 shows the output signal of each of the index finger designs, which was acquired with the oscilloscope.

(a) Ring Finger Design. (b) Finger with Plane Design. (c) TPU Finger Design. (d) Flat Finger Design.

Figure 5.19: Execution of Finger Tapping Tests Using Different Index Finger Designs.

The "Ring Finger" design generated the highest peak-to-peak voltage and had the largest contact area among all tested designs. This design proved to be comfortable and effectively prevented any displacement during the tests. The "Finger with Plane" design was the most successful, as it allowed the entire index finger to be securely attached to the piece, with no displacement observed during the FT test. However, due to its smaller contact area compared to the "Ring Finger" design, the OV recorded was correspondingly lower. The remaining designs produced the lowest OV values. While the "Flat Finger" design was still considered viable, the same could not be said for the "TPU Finger" design (for which the contact area could not be calculated, since it has a cylinder shape, causing a contact area variation), which did not perform as well.

Table 5.6: Results of Peak-to-Peak Voltage for Finger-Tapping With Different Index Finger's Designs.

Index Finger Design	**Impact Area (cm^2)**	**Peak-to-Peak Voltage ± SD (V)**
Ring Finger	16.56	2.1 ± 0.3
Finger with Plane	10.07	1.3 ± 0.2
Flat Finger	11.96	0.7 ± 0.1
TPU Finger	-	0.5 ± 0.1

Consequently, the final prototype for the index finger was a hybrid, combining the secure attachment of the "Finger with Plane" design with the larger contact area of the "Ring Finger" design.

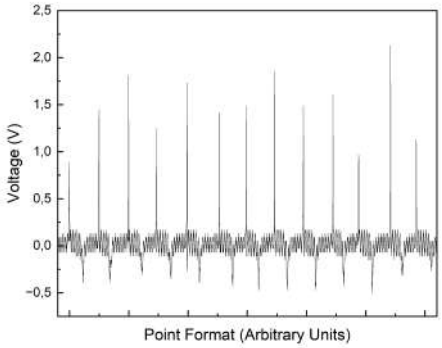

(a) Ring Finger.

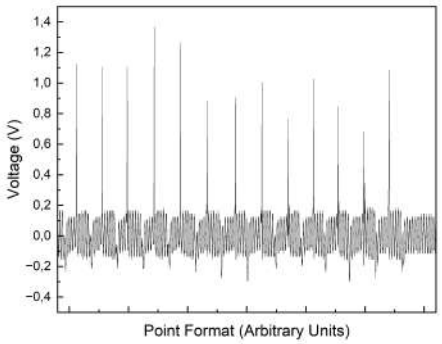

(b) Finger with Plane.

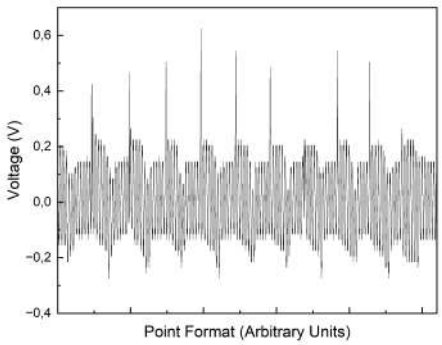

(c) Flat Finger.

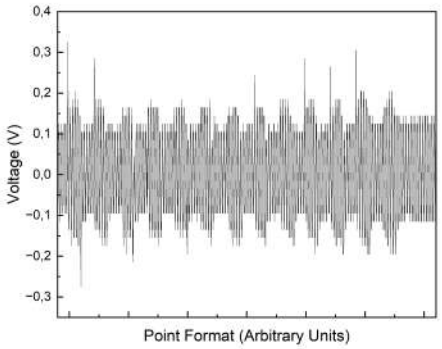

(d) TPU Finger.

Figure 5.20: Finger Tapping Tests for Different Index Finger Designs.

Finally, tremor was simulated using the wristband shown in Figure 5.9. The detected signal can be seen in Figure 5.21. It was not possible to evaluate individual peaks, and only a high degree of tremor could be detected. Even so, it was possible to distinguish tremor from a resting position, demonstrating the developed sensors can be used as valuable tools for monitoring PD progression.

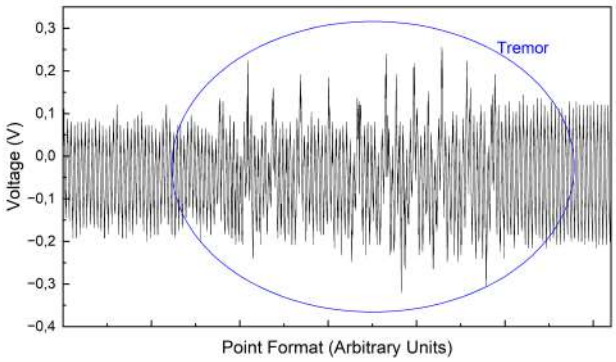

Figure 5.21: Output Voltage Resultant of Emulated Tremor Using Wristband Prototype.

6

Conclusion and Future Work

In line with the lack of objective ways to monitor Parkinson's Disease progression and the effectiveness of medication, a 3D-printed sensor based on the triboelectric and piezoelectric effects was developed. The initial phase involved studying different active layer designs, such as the ones mentioned on Table 4.1, and electrode configurations to gain a deeper understanding of how geometry and materials influence the output voltage of a device based on the triboelectric effect. Later, a thermal bath method was conducted in order to synthesize ZnO on 3D-Printed samples made of TPU, to improve the sensor's sensitivity by incorporating this piezoelectric material in the device's structure.

Different impact forces were tested (between 30 N and 60 N), the detection limits were evaluated using weights between 5 g and 200 g, and it was proven that ZnO's presence enhances the sensor's output voltage. A final prototype was developed using conductive filaflex as an electrode and TPU as an active layer where zinc-based materials were grown. The final prototype successfully detected finger-tapping movements, allowing the assessment of movement frequency, force and rhythm. Additionally, a wristband designed to detect tremor movements was developed using the same materials and principles. However, this prototype was not sensitive enough to detect mild tremor.

Future work could focus on improving the FT sensor to provide more accurate and reliable results. Exploring alternative 3D-printing polymers, such as PDMS, which is commonly cited in literature, may offer new insights into material performance. Moreover, increasing the synthesis temperature of ZnO should be considered to determine the optimal temperature that maximizes the output voltage. Testing the growth of other metal oxides, such as zinc-tin oxide, could also be a viable approach, as it would allow for an evaluation of which materials offer better adhesion to the substrate and which contribute to an increase in output voltage.

Furthermore, integrating a real-time data acquisition circuit connected to a smartphone would ease the test procedure and allow patients to perform this task at home. Implementing machine learning algorithms could automatically distinguish the finger-tapping patterns of a healthy individual from those of a Parkinson's Disease patient. Additionally, algorithms that automatically calculate peak-to-peak voltage, tapping frequency, and

amplitude would facilitate the device's usability.

Further advancements could also focus on improving the wristband to enhance its sensitivity, making it capable of detecting mild tremors, thus expanding its utility. One approach could involve increasing the surface area of the active layer, as well as testing other flexible filaments and metal oxides.

By incorporating these improvements, the device could become a versatile tool for monitoring Parkinson's Disease, offering both diagnostic and therapeutic benefits.

The manufacturing process for developing the sensors is simple and cost-effective, allowing for easy customization to meet individual user needs. It holds significant potential as a valuable tool for objectively monitoring patients with Parkinson's Disease, enabling its use not only during doctor appointments but also in the comfort of the patient's home.

Bibliography

[1] J. M. Lourenço. *The NOVAthesis LaTeX Template User's Manual*. NOVA University Lisbon. 2021. URL: https://github.com/joaomlourenco/novathesis/raw/main/template.pdf (cit. on p. i).

[2] World Health Organization. *Parkinson disease*. 2023. URL: https://www.who.int/news-room/fact-sheets/detail/parkinson-disease (visited on 2024) (cit. on p. 1).

[3] E. R. Dorsey et al. "The Emerging Evidence of the Parkinson Pandemic". In: 8 (2018), pp. 3–8. DOI: 10.3233/JPD-181474 (cit. on p. 1).

[4] R. Bremm et al. "Sensor-Based Quantification of MDS-UPDRS III Subitems in Parkinson's Disease Using Machine Learning". In: *Sensors* 24 (2024-03), p. 2195. DOI: 10.3390/s24072195 (cit. on pp. 1, 2, 11).

[5] S. Latif et al. "Dopamine in Parkinson's disease". In: *Clinica Chimica Acta* 522 (2021), pp. 114–126. ISSN: 0009-8981. DOI: https://doi.org/10.1016/j.cca.2021.08.009. URL: https://www.sciencedirect.com/science/article/pii/S000989812100276X (cit. on p. 1).

[6] J. Jankovic. "Parkinson ' s disease : clinical features and diagnosis". In: 1957 (2008), pp. 368–376. DOI: 10.1136/jnnp.2007.131045 (cit. on p. 1).

[7] W. Liu et al. "Vision-based estimation of MDS-UPDRS scores for quantifying Parkinson ' s disease tremor severity". In: *Medical Image Analysis* 85.January (2023), p. 102754. ISSN: 1361-8415. DOI: 10.1016/j.media.2023.102754. URL: https://doi.org/10.1016/j.media.2023.102754 (cit. on p. 1).

[8] L. F. Sigcha et al. "Deep learning and wearable sensors for the diagnosis and monitoring of Parkinson's disease: A systematic review". In: *Expert Systems with Applications* Volume 229, Part A (2023-05), p. 120541. DOI: 10.1016/j.eswa.2023.120541 (cit. on pp. 1, 2).

[9] A. C. K. A. "Update on the diagnosis and management of Parkinson ' s disease". In: 20.4 (2020), pp. 393–398. DOI: 10.7861/clinmed.2020-0220 (cit. on p. 1).

[10] S. H. G. Berendsen, J. Meuwese, and L. Schoenmakers. "The correlation between outcome measures of smartwatch data and MDS-UPDRS part-III scores in parkinson's disease patients". In: (2023-06). URL: http://essay.utwente.nl/95209/ (cit. on p. 1).

[11] A. Regnault et al. "Does the MDS - UPDRS provide the precision to assess progression in early Parkinson's disease Learnings from the Parkinson ' s progression marker initiative cohort". In: *Journal of Neurology* 266.8 (2019), pp. 1927–1936. ISSN: 1432-1459. DOI: 10.1007/s00415-019-09348-3. URL: https://doi.org/10.1007/s00415-019-09348-3 (cit. on p. 1).

[12] C. G. Goetz et al. "Movement Disorder Society-sponsored revision of the Unified Parkinson's Disease Rating Scale (MDS-UPDRS): Scale presentation and clinimetric testing results". In: *Movement Disorders* 23.15 (2008), pp. 2129–2170. DOI: https://doi.org/10.1002/mds.22340. eprint: https://movementdisorders.onlinelibrary.wiley.com/doi/pdf/10.1002/mds.22340. URL: https://movementdisorders.onlinelibrary.wiley.com/doi/abs/10.1002/mds.22340 (cit. on pp. 1, 2).

[13] Y. Guo et al. "Movement Disorder Society Unified Parkinson's Disease Rating Scale Motor Examination Retains Its 2-Domain Profile in Both and States". In: *Movement Disorders Clinical Practice* 9.8 (2022), pp. 1149–1151. DOI: https://doi.org/10.1002/mdc3.13566. eprint: https://movementdisorders.onlinelibrary.wiley.com/doi/pdf/10.1002/mdc3.13566. URL: https://movementdisorders.onlinelibrary.wiley.com/doi/abs/10.1002/mdc3.13566 (cit. on pp. 1, 2).

[14] A. S. Chandrabhatla, I. J. Pomeraniec, and A. Ksendzovsky. "Co-evolution of machine learning and digital technologies to improve monitoring of Parkinson's disease motor symptoms". In: *NPJ Digital Medicine* 5.1 (2022), p. 32. DOI: 10.1038/s41746-022-00568-y. URL: https://www.nature.com/articles/s41746-022-00568-y (cit. on p. 2).

[15] J. J. Elm et al. "Feasibility and utility of a clinician dashboard from wearable and mobile application Parkinson's disease data". In: *NPJ Digital Medicine* 2 (2019), p. 95. DOI: 10.1038/s41746-019-0169-y. URL: https://www.nature.com/articles/s41746-019-0169-y (cit. on pp. 2, 11).

[16] B. Vescio et al. "Wearable Devices for Assessment of Tremor". In: 12.June (2021), pp. 1–7. DOI: 10.3389/fneur.2021.680011 (cit. on p. 2).

[17] Z. L. Wang. "Triboelectric Nanogenerators as New Energy Technology for Self-Powered Systems and as Active Mechanical and Chemical Sensors". In: *ACS Nano* 7.11 (2013), pp. 9533–9557. ISSN: 1936-0851. DOI: 10.1021/nn404614z. URL: https://doi.org/10.1021/nn404614z (cit. on p. 2).

[18] K. V. Wong and A. Hernandez. "A Review of Additive Manufacturing". In: 2012 (2012). DOI: 10.5402/2012/208760 (cit. on pp. 3, 4).

[19] H. Bikas, P. Stavropoulos, and G. Chryssolouris. "Additive manufacturing methods and modelling approaches : a critical review". In: (2016), pp. 389–405. DOI: 10.1007/s00170-015-7576-2 (cit. on p. 3).

[20] N. Li et al. "Journal of Materials Science and Technology Progress in additive manufacturing on new materials : A review". In: *Journal of Materials Science and Technology* 35.2 (2018), pp. 242–269. ISSN: 1005-0302. DOI: 10.1016/j.jmst.2018.09.002. URL: https://doi.org/10.1016/j.jmst.2018.09.002 (cit. on p. 3).

[21] P. Dudek. "Agh university of science and technology, faculty of mechanical engineering and robotics, al. a. mickiewicza 30, 30-059 kraków, poland". In: (2013). DOI: 10.2478/amm-2013-0186 (cit. on p. 3).

[22] M. Davoudi, C. Y. An, and D. E. Kim. "A Review on Triboelectric Nanogenerators, Recent Applications, and Challenges". In: *International Journal of Precision Engineering and Manufacturing-Green Technology* 11.5 (2024), pp. 1317–1340. DOI: 10.1007/s40684-023-00569-6 (cit. on p. 4).

[23] M. A. P. Mahmud et al. "3D-Printed Triboelectric Nanogenerators : State of the Art , Applications , and Challenges". In: (2021), pp. 99–102. DOI: 10.1002/aesr.202000045 (cit. on pp. 4, 5, 26).

[24] H. Zhao et al. "Wearable sensors and features for diagnosis of neurodegenerative diseases : A systematic review". In: (2023). DOI: 10.1177/20552076231173569 (cit. on pp. 4, 7).

[25] A. Mathew, A. Chandrasekhar, and V. Shanmugasundaram. "A review on real-time implantable and wearable health monitoring sensors based on triboelectric nanogenerator approach". In: *Nano Energy* 80 (2021-02), p. 105566. DOI: 10.1016/j.nanoen.2020.105566 (cit. on pp. 4, 5).

[26] Z. Zhao et al. "From Body Monitoring to Biomolecular Sensing: Current Progress and Future Perspectives of Triboelectric Nanogenerators in Point-of-Care Diagnostics". In: *Sensors* 24.2 (2024). ISSN: 1424-8220. DOI: 10.3390/s24020511. URL: https://www.mdpi.com/1424-8220/24/2/511 (cit. on p. 6).

[27] H. Zou et al. "Quantifying the triboelectric series". In: 2019 (), pp. 1–9. DOI: 10.1038/s41467-019-09461-x (cit. on pp. 6, 63).

[28] Z. Kinas et al. "High-performance triboelectric nanogenerator based on carbon nanomaterials functionalized polyacrylonitrile nanofibers". In: *Energy* 239 (2022), p. 122369. ISSN: 0360-5442. DOI: https://doi.org/10.1016/j.energy.2021.122369. URL: https://www.sciencedirect.com/science/article/pii/S0360544221026189 (cit. on pp. 6, 14).

[29] R. Zhang and H. Olin. "Material choices for triboelectric nanogenerators : A critical review". In: September (2020), pp. 1–13. DOI: 10.1002/eom2.12062 (cit. on p. 6).

[30] A. dos Santos et al. "Transduction Mechanisms, Micro-Structuring Techniques, and Applications of Electronic Skin Pressure Sensors: A Review of Recent Advances". In: *Sensors* 20 (2020-08), p. 4407. DOI: 10.3390/s20164407 (cit. on p. 7).

[31] J. F. Tressler, S. Alkoy, and R. E. Newnham. "Piezoelectric Sensors and Sensor Materials". In: (1998) (cit. on p. 7).

[32] B. Bera and M. D. Sarkar. "Piezoelectric Effect , Piezotronics and Piezophototronics : A Review". In: *Imperial Journal of Interdisciplinary Research (IJIR)* 2.11 (2016), pp. 1407–1410. ISSN: 2454-1362 (cit. on p. 7).

[33] A. Mayeen and N. Kalarikkal. "2 - Development of ceramic-controlled piezoelectric devices for biomedical applications". In: *Fundamental Biomaterials: Ceramics*. Ed. by S. Thomas, P. Balakrishnan, and M. Sreekala. Woodhead Publishing Series in Biomaterials. Woodhead Publishing, 2018, pp. 47–62. ISBN: 978-0-08-102203-0. DOI: https://doi.org/10.1016/B978-0-08-102203-0.00002-0. URL: https://www.sciencedirect.com/science/article/pii/B9780081022030000020 (cit. on pp. 7, 8).

[34] K. Kim et al. "Review Article Static Force Measurement Using Piezoelectric Sensors". In: *Journal of Sensors* 2021 (2021). DOI: 10.1155/2021/6664200 (cit. on p. 7).

[35] S. M. Hosseini, H. Kalhori, and A. Al-jumaily. "Active vibration control in human forearm model using paired piezoelectric sensor and actuator". In: June 2020 (2021). DOI: 10.1177/1077546320957533 (cit. on p. 7).

[36] S. Kazi et al. "Experimental Implementation of Smart Glove Incorporating Piezoelectric Actuator for Hand Tremor Control". In: *WSEAS Transactions on Systems and Control* 5.6 (2010), pp. 443–453. URL: https://api.semanticscholar.org/CorpusID:4682659 (cit. on p. 7).

[37] S. M. K. Fereshteh Talaei. "Design and Fabrication of a Device for Reducing Hand Tremor in Parkinson Patients during Eating". In: (2023), pp. 21–28. DOI: 10.4103/jmss.jmss (cit. on p. 7).

[38] X. Wang et al. "A flexible triboelectric-piezoelectric hybrid nanogenerator based on P(VDF-TrFE) nanofibers and PDMS/MWCNT for wearable devices". In: *Scientific Reports* 6.November (2016), pp. 1–10. ISSN: 20452322. DOI: 10.1038/srep36409 (cit. on p. 8).

[39] H. Patnam, S. A. Graham, and J. S. Yu. "Y - ZnO Micro fl owers Embedded Polymeric Composite Films to Enhance the Electrical Performance of Piezo/Tribo Hybrid Nanogenerators for Biomechanical Energy Harvesting and Sensing Applications". In: (2021). DOI: 10.1021/acssuschemeng.1c00025 (cit. on pp. 8, 12, 13).

[40] B. Kumar and S.-w. Kim. "Energy harvesting based on semiconducting piezoelectric ZnO nanostructures". In: (2012), pp. 342–355. DOI: 10.1016/j.nanoen.2012.02.001 (cit. on p. 8).

[41] P. Supraja et al. "Study of ZnO nanosheets growth parameters effect on the performance of the triboelectric nanogenerator". In: *Materials Today: Proceedings* xxxx (2023), pp. 2–7. ISSN: 22147853. DOI: 10.1016/j.matpr.2023.02.087. URL: https://doi.org/10.1016/j.matpr.2023.02.087 (cit. on pp. 8, 9).

[42] S. Ferreira et al. "Porous ZnO Nanostructures Synthesized by Microwave Hydrothermal Method for Energy Harvesting Applications". In: (2021-05), https://www.intechopen.com first/porous. DOI: 10.5772/intechopen.97060 (cit. on p. 8).

[43] J. Malik et al. *ZnO Nanoparticles : Growth , Properties , and Applications ZnO Nanoparticles : Growth , Properties , and Applications*. Vol. 5. 2015, pp. 1–36. ISBN: 1588831701 (cit. on p. 8).

[44] Y. Wang et al. "Fundamentals and Applications of ZnO-Nanowire-Based Piezotronics and Piezo-Phototronics". In: *Micromachines* 14.1 (2023). ISSN: 2072-666X. DOI: 10.3390/mi14010047. URL: https://www.mdpi.com/2072-666X/14/1/47 (cit. on p. 8).

[45] M. A. Borysiewicz. "ZnO as a Functional Material, a Review". In: *Crystals* 9.10 (2019). ISSN: 2073-4352. DOI: 10.3390/cryst9100505. URL: https://www.mdpi.com/2073-4352/9/10/505 (cit. on p. 8).

[46] M. Saeed et al. "Recent Advances, Challenges, and Future Perspectives of ZnO Nanostructure Materials Towards Energy Applications". In: *Chemical Record* 24.1 (2024). ISSN: 15280691. DOI: 10.1002/tcr.202300106 (cit. on p. 8).

[47] L. Schmidt-Mende and J. L. MacManus-Driscoll. "ZnO – nanostructures, defects, and devices". In: *Materials Today* 10.5 (2007), pp. 40–48. ISSN: 1369-7021. DOI: https://doi.org/10.1016/S1369-7021(07)70078-0. URL: https://www.sciencedirect.com/science/article/pii/S1369702107700780 (cit. on p. 8).

[48] Y. Li et al. "Development of conductive materials and conductive networks for flexible force sensors". In: *Chemical Engineering Journal* 455 (2023), p. 140763. ISSN: 1385-8947. DOI: 10.1016/j.cej.2022.140763. URL: https://www.sciencedirect.com/science/article/pii/S138589472206243X (cit. on p. 9).

[49] D. Zhao et al. "Flexible Sensors Based on Conductive Polymer Composites". In: *Sensors* 24.14 (2024). ISSN: 1424-8220. DOI: 10.3390/s24144664. URL: https://www.mdpi.com/1424-8220/24/14/4664 (cit. on p. 9).

[50] M. Ramesh et al. "Nanotechnology-Enabled Biosensors: A Review of Fundamentals, Design Principles, Materials, and Applications". In: *Biosensors (Basel)* 13.1 (2022-12), p. 40. DOI: 10.3390/bios13010040 (cit. on p. 9).

[51] J. Phiri, P. Gane, and T. C. Maloney. "General overview of graphene: Production, properties and application in polymer composites". In: *Materials Science and Engineering: B* 215 (2017), pp. 9–28. ISSN: 0921-5107. DOI: https://doi.org/10.1016/j.mseb.2016.10.004. URL: https://www.sciencedirect.com/science/article/pii/S0921510716301568 (cit. on p. 9).

[52] R. Ye, D. K. James, and J. M. Tour. "Laser-Induced Graphene: From Discovery to Translation". In: *Advanced Materials* (2018), p. 1803621. DOI: 10.1002/adma.201803621 (cit. on p. 9).

[53] T. Pinheiro et al. "Water Peel-Off Transfer of Electronically Enhanced, Paper-Based Laser-Induced Graphene for Wearable Electronics". In: *ACS Nano* 16.12 (2022). PMID: 36383513, pp. 20633–20646. DOI: 10.1021/acsnano.2c07596. eprint: https://doi.org/10.1021/acsnano.2c07596. URL: https://doi.org/10.1021/acsnano.2c07596 (cit. on pp. 9, 15).

[54] C. Chung et al. "Biomedical Applications of Graphene and Graphene Oxide". In: *Accounts of Chemical Research* 46.10 (2013), pp. 2211–2224. DOI: 10.1021/ar300159f (cit. on p. 9).

[55] J. Coelho et al. "Paper-based laser-induced graphene for sustainable and flexible microsupercapacitor applications". In: *Microchimica Acta* 190.1 (2022-12), p. 40. ISSN: 1436-5073. DOI: 10.1007/s00604-022-05610-0. URL: https://doi.org/10.1007/s00604-022-05610-0 (cit. on pp. 9, 15).

[56] J. Amo-Salas et al. "Computer Vision for Parkinson's Disease Evaluation: A Survey on Finger Tapping". In: *Healthcare* 12.4 (2024). ISSN: 2227-9032. DOI: 10.3390/healthcare12040439. URL: https://www.mdpi.com/2227-9032/12/4/439 (cit. on p. 10).

[57] A. Zhuparris et al. "Treatment Detection and Movement Disorder Society-Uni fi ed Parkinson ' s Disease Rating Scale , Part III Estimation Using Finger Tapping Tasks". In: 38.10 (2023), pp. 1795–1805. DOI: 10.1002/mds.29520 (cit. on p. 10).

[58] D. C. Aucineia Ferreira Marco Branco. "Teste de Batidas do Dedo em Idosos Portadores de Alzheimer". In: (2016), pp. 307–312. DOI: 10.25746/ruiips.v4.i2.9939 (cit. on p. 10).

[59] B. N. Axelrod, J. E. Meyers, and J. J. Davis. "Finger Tapping Test Performance as a Measure of Performance Validity". In: *Journal Name* (2014-09). Accessed September 2015. DOI: 10.1080/13854046.2014.907583 (cit. on p. 10).

[60] S. M. 25. *The Neurological Exam: Finger Tapping*. Accessed: 2024-08-01. 2023. URL: https://www.youtube.com/watch?v=cxHpFWKIfGw&ab_channel=StanfordMedicine25 (cit. on p. 10).

[61] D. M. Herz and P. Brown. "Moving, Fast and Slow: Behavioural Insights into Bradykinesia in Parkinson's Disease". In: *Brain* 146.9 (2023), pp. 3576–3586. ISSN: 0006-8950. DOI: 10.1093/brain/awad069. URL: https://doi.org/10.1093/brain/awad069 (cit. on p. 10).

[62] S. E. Romero et al. "A pilot study for testing a low-cost 3D design with an inertial sensor for the quantitative assessment of finger tapping in patients with Parkinson's Disease". In: (2023), pp. 1–4. DOI: 10.1109/EMBC40787.2023.10340532 (cit. on pp. 10, 11).

[63] V. Ravichandran et al. "iTex Gloves: Design and In-Home Evaluation of an E-Textile Glove System for Tele-Assessment of Parkinson's Disease". In: *Sensors (Basel)* 23.6 (2023), p. 2877. ISSN: 1424-8220. DOI: 10.3390/s23062877. URL: https://doi.org/10.3390/s23062877 (cit. on p. 11).

[64] S. Tripathi et al. "Clinical Review of Smartphone Applications in Parkinson's Disease". In: *The Neurologist* 27.4 (2022-07), pp. 183–193. ISSN: 2331-2637. DOI: 10.1097/NRL.0000000000000413 (cit. on p. 11).

[65] P. Li et al. "The role of wrist-worn technology in the management of Parkinson's disease in daily life: A narrative review". In: *Frontiers in Neuroinformatics* 17 (2023), p. 1135300. DOI: 10.3389/fninf.2023.1135300. URL: https://www.frontiersin.org/articles/10.3389/fninf.2023.1135300/full (cit. on p. 11).

[66] D. L. Guarín et al. "Characterizing Disease Progression in Parkinson's Disease from Videos of the Finger Tapping Test". In: *IEEE Transactions on Neural Systems and Rehabilitation Engineering* 32 (2024), pp. 2293–2301. DOI: 10.1109/TNSRE.2024.3416446 (cit. on p. 11).

[67] S. Kajan et al. "Real-time visual verification of leap motion controller measurements for reliable finger tapping test in Parkinson's disease". In: *Journal of Electrical Engineering* 75 (2024-08), pp. 325–332. DOI: 10.2478/jee-2024-0039 (cit. on p. 11).

[68] M. Yokoe et al. "Opening velocity, a novel parameter, for finger tapping test in patients with Parkinson's disease". In: *Parkinsonism & Related Disorders* 15.6 (2009), pp. 440–444. ISSN: 1873-5126. DOI: 10.1016/j.parkreldis.2008.11.003. URL: https://doi.org/10.1016/j.parkreldis.2008.11.003 (cit. on p. 11).

[69] K. Niazmand et al. "Quantitative Evaluation of Parkinson ' s Disease using sensor based smart Glove". In: *2011 24th International Symposium on Computer-Based Medical Systems (CBMS)* (), pp. 1–8. DOI: 10.1109/CBMS.2011.5999113 (cit. on p. 11).

[70] D. F. Vera et al. "Flexible Forearm Triboelectric Sensors for Parkinson's Disease Diagnosing and Monitoring". In: *Proceedings of the Annual International Conference of the IEEE Engineering in Medicine and Biology Society, EMBS* 2022-July (2022), pp. 4909–4912. ISSN: 1557170X. DOI: 10.1109/EMBC48229.2022.9871644 (cit. on pp. 11, 13).

[71] D. V. Anaya and M. R. Yuce. "Stretchable triboelectric sensor for measurement of the forearm muscles movements and fingers motion for Parkinson ' s disease assessment and assisting technologies". In: August 2020 (2021), pp. 1–12. DOI: 10.1002/mds3.10154 (cit. on p. 12).

[72] R. I. Haque et al. "Nano Energy Self-powered triboelectric touch sensor made of 3D printed materials". In: *Nano Energy* 52.June (2018), pp. 54–62. ISSN: 2211-2855. DOI: 10.1016/j.nanoen.2018.07.038. URL: https://doi.org/10.1016/j.nanoen.2018.07.038 (cit. on pp. 12, 13).

[73] P. Kumbhakar et al. "Energy Harvesting Using ZnO Nanosheet-Decorated 3D-Printed Fabrics". In: (2023). DOI: 10.1021/acsami.3c08374 (cit. on pp. 12, 13, 17, 32).

[74] P. Kumbhakar et al. "Quantifying instant water cleaning efficiency using zinc oxide decorated complex 3D printed porous architectures". In: *Journal of Hazardous Materials* 418.March (2021), p. 126383. ISSN: 0304-3894. DOI: 10.1016/j.jhazmat.2021.126383. URL: https://doi.org/10.1016/j.jhazmat.2021.126383 (cit. on p. 12).

[75] J. Li et al. "Thin , soft , 3D printing enabled crosstalk minimized triboelectric nanogenerator arrays for tactile sensing". In: 3 (2023), pp. 111–117. DOI: 10.1016/j.fmre.2022.01.021 (cit. on p. 13).

[76] M. K. Yadav, D. Padalia, and N. Yadav. "Flexible piezoelectric polymer membrane as effective tactile sensor". In: *IEEE Journal on Flexible Electronics* PP.X (2024), p. 1. DOI: 10.1109/JFLEX.2024.3422258 (cit. on p. 13).

[77] A. Siddiqui, S. Das, and M. Bhattacharjee. "Sensors and Actuators : A . Physical Nanofillers embedded flexible piezoelectric polymer sensor pad for robotic and human finger tap analysis". In: *Sensors and Actuators: A. Physical* 375.March (2024), p. 115503. ISSN: 0924-4247. DOI: 10.1016/j.sna.2024.115503. URL: https://doi.org/10.1016/j.sna.2024.115503 (cit. on p. 13).

[78] K. Zhou et al. "Ultra-stretchable triboelectric nanogenerator as high-sensitive and self-powered electronic skins for energy harvesting and tactile sensing". In: *Nano Energy* 70.January (2020), p. 104546. ISSN: 22112855. DOI: 10.1016/j.nanoen.2020.104546. URL: https://doi.org/10.1016/j.nanoen.2020.104546 (cit. on p. 13).

[79] H. Xiang et al. "Carbon fibre reinforced triboelectric nanogenerator for self-powered sporting events monitoring". In: *Nano Energy* 123 (2024), p. 109403. ISSN: 2211-2855. DOI: https://doi.org/10.1016/j.nanoen.2024.109403. URL: https://www.sciencedirect.com/science/article/pii/S2211285524001514 (cit. on p. 14).

[80] *Conductive Filaflex - Electrically Conductive Flexible TPU Filament*. https://recreus.com/gb/filaments/3-filaflex-conductivo.html. Accessed: 25-Sep-2024. Recreus Industries, S.L., 2024 (cit. on p. 14).

[81] J. Cheng et al. "Locally Controllable Laser Patterning Transfer of Thermoplastic Polyurethane Induced by Sustainable Bismuth Trioxide Substrate". In: *Applied Surface Science* 550 (2021-02), p. 149299. DOI: 10.1016/j.apsusc.2021.149299 (cit. on p. 15).

[82] Z. Cao et al. "Laser-induced blackening on surfaces of thermoplastic polyurethane/BiOCl composites". In: *Polymer Degradation and Stability* 141 (2017-05). DOI: 10.1016/j.polymdegradstab.2017.05.004 (cit. on p. 15).

[83] J. Lee and H. So. "3D-printing-assisted flexible pressure sensor with a concentric circle pattern and high sensitivity for health monitoring". In: *Microsystems and Nanoengineering* 9.1 (2023). ISSN: 20557434. DOI: 10.1038/s41378-023-00509-z (cit. on p. 16).

[84] Y. Kim, H. Yang, and J. H. Oh. "Simple fabrication of highly sensitive capacitive pressure sensors using a porous dielectric layer with cone-shaped patterns". In: *Materials and Design* 197 (2021), p. 109203. ISSN: 18734197. DOI: 10.1016/j.matdes.2020.109203. URL: https://doi.org/10.1016/j.matdes.2020.109203 (cit. on p. 16).

[85] S. Cao et al. "A Flexible and Highly Sensitive Capacitive Pressure Sensor With Microstructured Dielectric TPU Layer Based on Mesh Fabric as Template". In: *IEEE Sensors Journal* 22.21 (2022), pp. 20276–20284. ISSN: 15581748. DOI: 10.1109/JSEN.2022.3207005 (cit. on p. 16).

[86] H. J. Lee et al. "Wearable Triboelectric Strain-Insensitive Pressure Sensors Based on Hierarchical Superposition Patterns". In: *ACS Sensors* 6.6 (2021), pp. 2411–2418. ISSN: 23793694. DOI: 10.1021/acssensors.1c00640 (cit. on p. 16).

[87] A. Saletnik, B. Saletnik, and C. Puchalski. "Overview of Popular Techniques of Raman Spectroscopy and Their Potential in the Study of Plant Tissues". In: *Molecules* 26.6 (2021-03), p. 1537. DOI: 10.3390/molecules26061537 (cit. on p. 21).

[88] A. Naumenko et al. "Peculiarities of Raman spectra of polyurethane/carbon nanotube composite". In: *The European Physical Journal B* 85 (2012), pp. 1–6 (cit. on p. 21).

[89] M. Stroe et al. "Optical and Structural Properties of Composites Based on Poly(urethane) and TiO_2 Nanowires". In: *Materials* 16.4 (2023). ISSN: 1996-1944. DOI: 10.3390/ma16041742. URL: https://www.mdpi.com/1996-1944/16/4/1742 (cit. on p. 21).

[90] K. Bruckmoser and K. Resch. "Investigation of Ageing Mechanisms in Thermoplastic Polyurethanes by Means of IR and Raman Spectroscopy". In: *Macromolecular Symposia* 339.1 (2014), pp. 70–83. DOI: 10.1002/masy.201300140 (cit. on p. 21).

[91] V. Nava, M. L. Frezzotti, and B. Leoni. "Raman Spectroscopy for the Analysis of Microplastics in Aquatic Systems". In: *Applied Spectroscopy* 75.11 (2021), pp. 1341–1357. DOI: 10.1177/00037028211043119 (cit. on pp. 21, 23).

[92] I. Smaranda et al. "The Influence of the Ceramic Nanoparticles on the Thermoplastic Polymers Matrix: Their Structural, Optical, and Conductive Properties". In: *Polymers* 13.16 (2021). ISSN: 2073-4360. DOI: 10.3390/polym13162773. URL: https://www.mdpi.com/2073-4360/13/16/2773 (cit. on p. 22).

[93] A. Dychalska et al. "Study of CVD diamond layers with amorphous carbon admixture by Raman scattering spectroscopy". In: *MATERIALS SCIENCE-POLAND* 33 (2015-09). DOI: 10.1515/msp-2015-0067 (cit. on p. 23).

[94] S. Sufi et al. "Effect of magnetic field on carbon nanotubes and graphene structure synthesized at low pressure via arc discharge process". In: 2017-01. DOI: 10.1063/1.4978843 (cit. on p. 23).

[95] O. Beyssac and M. Lazzeri. "Application of Raman spectroscopy to the study of graphitic carbons in the Earth Sciences". In: *European Mineralogical Union Notes in Mineralogy* 12 (2012-01), pp. 415–454. DOI: 10.1180/EMU-notes.12.12 (cit. on p. 23).

[96] A. A. Bunaciu, E. G. UdriŞTioiu, and H. Y. Aboul-Enein. "X-ray diffraction: instrumentation and applications". In: *Critical reviews in analytical chemistry* 45.4 (2015), pp. 289–299. DOI: 10.1080/10408347.2014.949616 (cit. on p. 23).

[97] E. Ameh. "A review of basic crystallography and x-ray diffraction applications". In: *The international journal of advanced manufacturing technology* 105.7 (2019), pp. 3289–3302 (cit. on pp. 23, 24).

[98] M. Abbas et al. "Physicochemical Study of Eco-Friendly Sugar Palm Fiber Thermoplastic Polyurethane Composites". In: *Bioresources* 11 (2016-07), pp. 9438–9454. DOI: 10.15376/biores.11.4.9438-9454 (cit. on p. 24).

[99] Q. Muhammad et al. "Cost-Effective and Flexible Scalable Fabrication of WO3 UV Photodetectors with Enhanced Performance via Integrated LIG Electrodes". In: *Advanced Materials Technologies* 9 (2024-01). DOI: 10.1002/admt.202301650 (cit. on p. 24).

[100] E. Aparicio Martinez et al. "Salivary Glucose Detection with Laser Induced Graphene/AgNPs Non-Enzymatic Sensor". In: *Biosensors* 13 (2023-01), p. 207. DOI: 10.3390/bios13020207 (cit. on p. 24).

[101] R. R. A. Soares et al. "Insights into solid-contact ion-selective electrodes based on laser-induced graphene: Key performance parameters for long-term and continuous measurements". In: *Microchimica Acta* 191.10 (2024), p. 615. DOI: 10.1007/s00604-024-06672-y. URL: https://doi.org/10.1007/s00604-024-06672-y (cit. on p. 27).

[102] P. Gill, T. T. Moghadam, and B. Ranjbar. "Differential scanning calorimetry techniques: applications in biology and nanoscience". In: *Journal of Biomolecular Techniques* 21.4 (2010-12), pp. 167–193 (cit. on p. 31).

[103] J. Slapnik et al. "Overprinting of TPU onto PA6 Substrates: The Influences of the Interfacial Area, Surface Roughness and Processing Parameters on the Adhesion between Components". In: *Polymers* 16.5 (2024). ISSN: 2073-4360. DOI: 10.3390/polym16050650. URL: https://www.mdpi.com/2073-4360/16/5/650 (cit. on p. 31).

[104] P. Kasprzyk, E. Sadowska, and J. Datta. "Investigation of Thermoplastic Polyurethanes Synthesized via Two Different Prepolymers". In: *Journal of Polymers and the Environment* 27.11 (2019), pp. 2588–2599. ISSN: 1572-8919. DOI: 10.1007/s10924-019-01543-7. URL: https://doi.org/10.1007/s10924-019-01543-7 (cit. on p. 31).

[105] F.-Y. Zhu et al. "3D nanostructure reconstruction based on the SEM imaging principle, and applications". In: *Nanotechnology* 25.18 (2014), p. 185705. DOI: 10.1088/0957-4484/25/18/185705 (cit. on p. 32).

[106] Q. Wang et al. "Two-dimensional ZnO nanosheets grown on flexible ITO-PET substrate for self-powered energy-harvesting nanodevices". In: *Applied Physics Letters* 112 (2018-02), p. 063906. DOI: 10.1063/1.5012950 (cit. on p. 33).

[107] A. Zhu et al. "Green Approach for Metal Oxide Deposition at an Air–Liquid–Solid Triphase Interface with Enhanced Photocatalytic Activity". In: *ACS Omega* 4 (2019-02), pp. 3534–3538. DOI: 10.1021/acsomega.8b03234 (cit. on p. 33).

[108] Y.-C. Liang, Y.-C. Chang, and W.-C. Zhao. "Design and Synthesis of Novel 2D Porous Zinc Oxide-Nickel Oxide Composite Nanosheets for Detecting Ethanol Vapor". In: *Nanomaterials* 10 (2020-10), p. 1989. DOI: 10.3390/nano10101989 (cit. on p. 33).

[109] V. Sharma et al. "Fabrication of innovative ZnO nanoflowers showing drastic biological activity". In: *New J. Chem.* 40 (2015-01). DOI: 10.1039/C5NJ02391B (cit. on p. 33).

[110] S. Borbón, S. Lugo, and I. López. "Fast synthesis of ZnO nanoflowers using a conductively heated sealed-vessel reactor without additives". In: *Materials Science in Semiconductor Processing* 91 (2019), pp. 310–315. ISSN: 1369-8001. DOI: https://doi.org/10.1016/j.mssp.2018.12.001. URL: https://www.sciencedirect.com/science/article/pii/S1369800118317633 (cit. on p. 33).

[111] A. N. P. Madathil, K. A. Vanaja, and M. K. Jayaraj. "Synthesis of ZnO nanoparticles by hydrothermal method". In: *Nanophotonic Materials IV*. Ed. by Z. Gaburro and S. Cabrini. Vol. 6639. International Society for Optics and Photonics. SPIE, 2007, 66390J. DOI: 10.1117/12.730364. URL: https://doi.org/10.1117/12.730364 (cit. on p. 33).

[112] P. Wang et al. "A facile cost-effective method for preparing poinsettia-inspired superhydrophobic ZnO nanoplate surface on Al substrate with corrosion resistance". In: *Applied Physics A* 122 (2016-01). DOI: 10.1007/s00339-016-9608-7 (cit. on p. 33).

[113] A. N. P. Madathil, K. A. Vanaja, and M. K. Jayaraj. "Synthesis of ZnO nanoparticles by hydrothermal method". In: *Nanophotonic Materials IV*. Ed. by Z. Gaburro and S. Cabrini. Vol. 6639. International Society for Optics and Photonics. SPIE, 2007, 66390J. DOI: 10.1117/12.730364. URL: https://doi.org/10.1117/12.730364 (cit. on p. 34).

[114] I. Musa, N. Qamhieh, and S. T. Mahmoud. "Synthesis and length dependent photoluminescence property of zinc oxide nanorods". In: *Results in Physics* 7 (2017), pp. 3552–3556. ISSN: 2211-3797. DOI: https://doi.org/10.1016/j.rinp.2017.09.035. URL: https://www.sciencedirect.com/science/article/pii/S2211379717311403 (cit. on p. 36).

A

Results of Peak-to-Peak Voltage of Different Electrodes

This appendix contains Table A.1, which regards the peak-to-peak voltages originated from sensors with different electrode materials combined with the "Square" design upon impact forces of 30 N, 40 N, 50 N and 60 N.

Table A.1: Results of Peak-to-Peak Voltage of Different Electrodes Combined with the Square Design Upon Impact Forces of 30 N, 40 N, 50 N and 60 N.

	Peak-to-Peak Voltage ± Standard Deviation (V)			
Pressure (kPa)	**Carbon Filaflex**	**Carbon Filaflex with LIG**	**TPU with LIG**	**Carbon Tape**
75	32 ± 2	10.1 ± 0.4	15 ± 1	4.7 ± 0.3
100	43 ± 2	19 ± 1	18 ± 1	6.9 ± 0.5
125	46 ± 2	22.4 ± 0.9	19 ± 2	9.0 ± 0.5
150	49 ± 4	28 ± 1	22 ± 1	11.5 ± 0.5

B

Scanning Electron Microscopy Results

This appendix contains Figure B.1 and Figure B.2 , regarding the SEM results of the designs with hexagons as protrusions ("Hexagons") and "Hexagon Holes", respectively. For both samples, ZnO synthesis was executed at 60 °C for 2 hours.

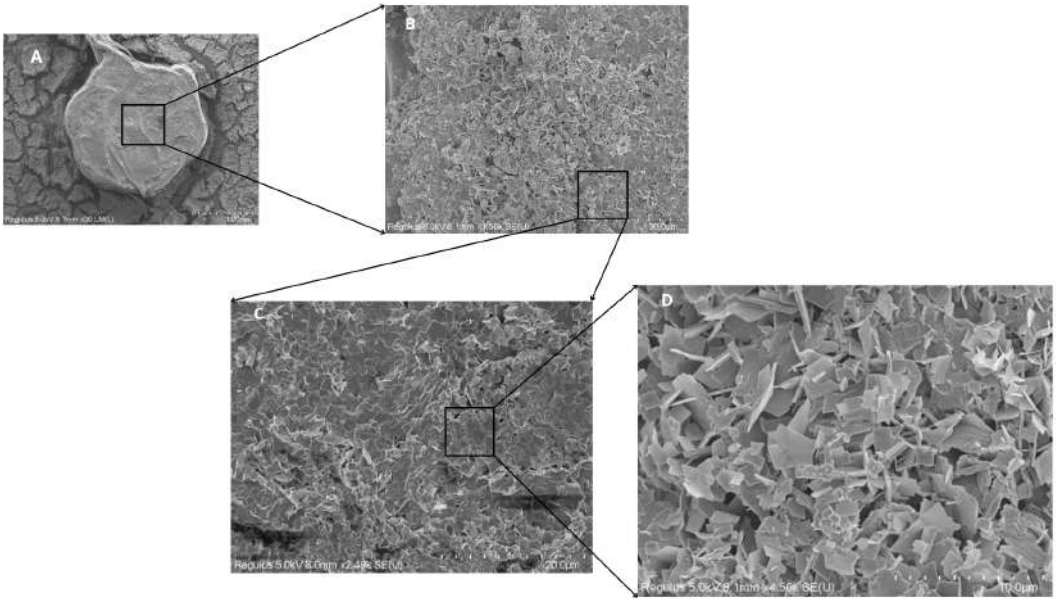

Figure B.1: SEM Images of "Hexagons" Sample Resulting from the Growth Process Performed at 60 °C for 2 Hours. (A) 30× Magnification, (B) 1.5× Magnification, (C) 2.5× Magnification, (D) 4.5× Magnification.

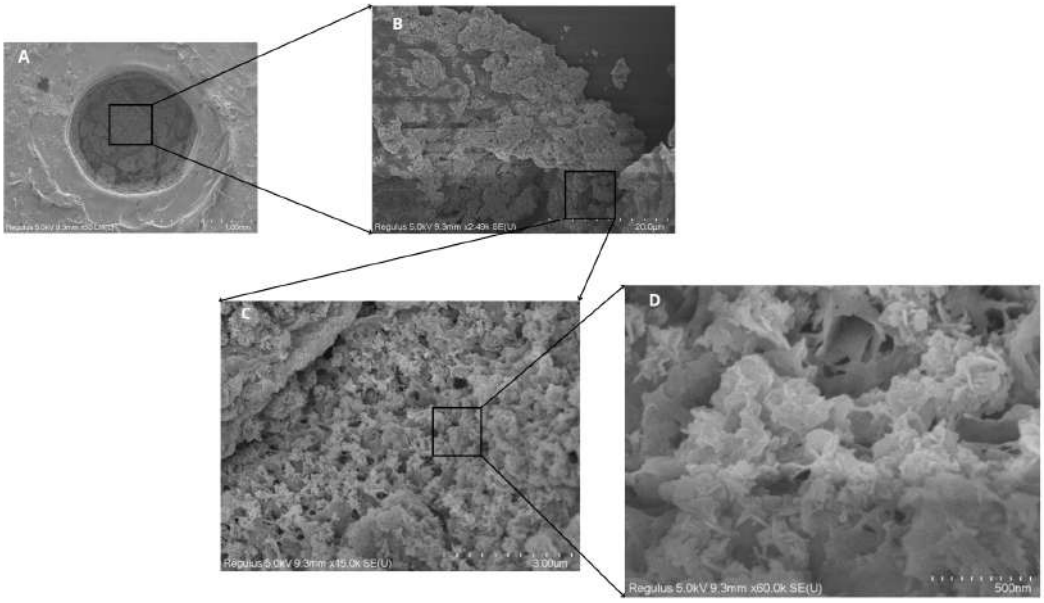

Figure B.2: SEM images of the "Hexagon Holes" Sample Resulting from the Growth Process Performed at 60 °C for 2 Hours. (A) 50× magnification, (B) 2.5× magnification, (C) 15× magnification, (D) 60× magnification.

C

Results of Peak-to-Peak Voltage for Different Designs

This appendix contains Table C.1, which regards the peak-to-peak voltages originated from sensors with different active layer patterns upon impact forces of 30 N, 40 N, 50 N and 60 N, using the CF Electrode.

Table C.1: Results of Peak-to-Peak Voltage for Different Designs Upon Impact Forces of 30 N, 40 N, 50 N and 60 N Using the CF Electrode.

	Peak-to-Peak Voltage for Each Pressure Impact ± Standard Deviation (V)			
	75 kPa	**100 kPa**	**125 kPa**	**150 kPa**
Square	33 ± 2	43 ± 2	46 ± 2	49 ± 4
Archimedean Circle	24 ± 3	28 ± 3	31 ± 3	32 ± 4
Spheres	8.1 ± 0.4	12.4 ± 0.5	19.2± 0.5	25.1 ± 0.5
Archimedean Square	5.5 ± 0.8	11.5 ± 0.7	14 ± 1	16 ± 1.0
Circle	4.7 ± 0.4	10.2 ± 0.5	13 ± 1	16 ± 2
Waves	3.2 ± 0.2	5.8 ± 0.2	6.4 ± 0.4	7.4 ± 0.3
Cones	4.8 ± 0.3	3.7 ± 0.3	3.7 ± 0.4	4.1 ± 0.5

D

Output Voltage for Prototype With and Without ZnO

This appendix includes the output voltage signal obtained for the prototype. Figure D.1 concerns the sample without ZnO, while Figure D.2 concerns the sample after the ZnO growing process. Both figures show the output from Tektronix Oscilloscope for 30 N, 40 N, 50 N and 60 N of impact force, respectively.

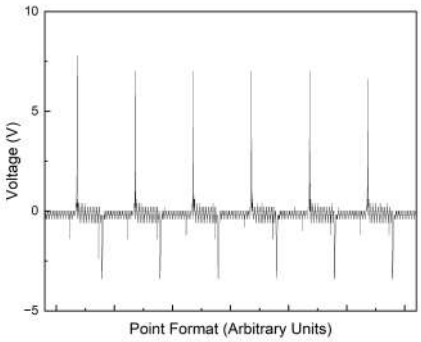

(a) 30 N

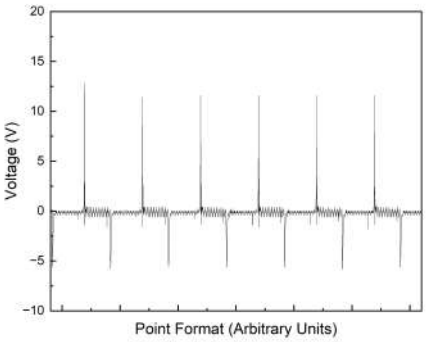

(b) 40 N

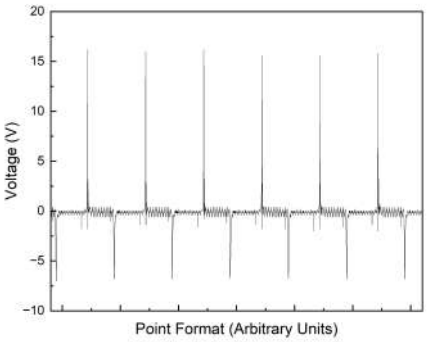

(c) 50 N

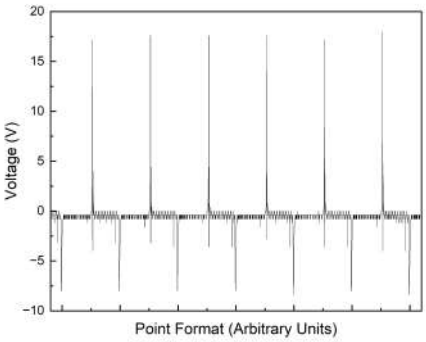

(d) 60 N

Figure D.1: Output Voltage for Prototype Without ZnO Upon an Impact Force of: (a) 30 N, (b) 40 N, (c) 50 N and (d) 60 N.

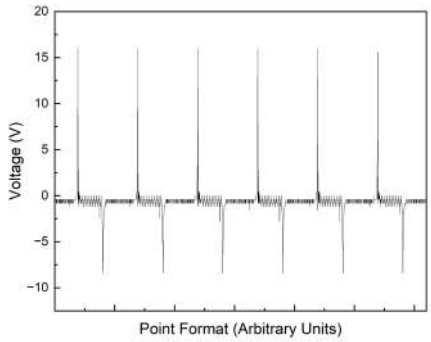

(a) 30 N

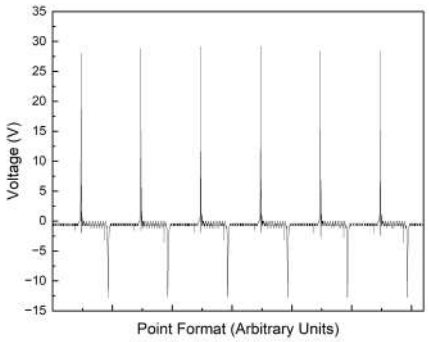

(b) 40 N

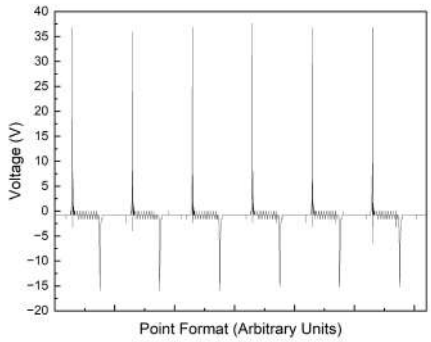

(c) 50 N

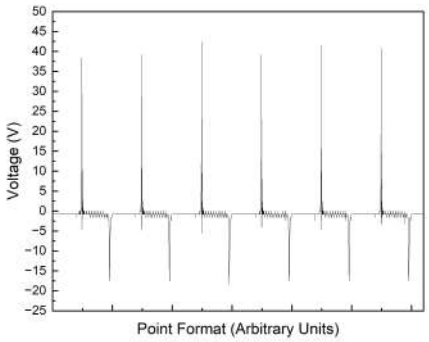

(d) 60 N

Figure D.2: Output Voltage for Prototype With ZnO Upon an Impact Force of: (a) 30 N, (b) 40 N, (c) 50 N and (d) 60 N.

I

Triboelectric Series

This annex contains a list of materials and their triboelectric charge density studied by Zou *et al.*, called Triboelectric Series.

Materials at the end of the table have a tendency to lose electrons, while materials from the top of the table have a tendency to attract electrons.

Table I.1: List of Materials Ordered According to Their TECD. Adapted from Zou *et al.* [27].

Material	**Average TECD** (μC m^{-2})	α
Chemical-resistant Viton fluoroelastomer rubber	-148.20	-1.31
Acetal	-143.33	-1.27
Flame-retardant Garolite	-142.76	-1.26
G-10 Garolite	-139.89	-1.24
Clear cellulose	-133.30	-1.18
Clear polyvinyl chloride (PVC)	-117.53	-1.04
Polytetrafluoroethylene (PTFE)	-113.06	-1.00
Abrasion-resistant polyurethane rubber	-109.22	-0.97
Acrylonitrile butadiene styrene (ABS)	-108.07	-0.96
Clear polycarbonate (glossy) (PC)	-104.63	-0.93
Polystyrene (PS)	-103.48	-0.92
Ultem polyetherimide (PE)	-102.91	-0.91
Polydimethylsiloxane (PDMS)	-102.05	-0.90
Polyester fabric (plain)	-101.48	-0.90
Electrical insulating Garolite that is easy to machine	-100.33	-0.89
High-temperature silicone rubber for food use	-94.03	-0.83
Polyimide film (Kapton)	-92.88	-0.82
Duralar polyester film (PET)	-89.44	-0.79
Polyvinylidene fluoride (PVDF)	-87.35	-0.77
Polyetheretherketone (PEEK)	-76.25	-0.67
Polyethylene (PE)	-71.20	-0.63
High-temperature silicone rubber	-69.95	-0.62
Wear-resistant Garolite	-68.51	-0.61
Low-density polyethylene (LDPE)	-67.94	-0.60
High-impact polystyrene	-67.37	-0.60
High-density polyethylene (HDPE)	-59.91	-0.53
Weather-resistant EPDM rubber	-53.61	-0.47
Leather strip (smooth)	-52.75	-0.47
Oil-filled cast nylon 6	-49.59	-0.44
Clear cast acrylic (PMMA)	-48.73	-0.43
Silicone	-47.30	-0.42
Abrasion-resistant SBR rubber	-40.13	-0.35
Flexible leather strip (smooth)	-34.40	-0.30
Noryl polyphenylene ether	-31.82	-0.28
Poly(phenylene Sulfide) (PPS)	-31.82	-0.28
Pigskin (smooth)	-30.10	-0.27
Polypropylene (PP)	-27.23	-0.24
Slippery nylon 66	-26.09	-0.23
Weather and chemical resistant Santoprene rubber	-25.23	-0.22
Chemical and vapor resistant Aflas rubber	-22.65	-0.20
Polysulfone	-28.92	-0.17
Cast nylon 6	-18.35	-0.16
Copy paper	-18.35	-0.16
Chemical-resistant and low-temperature fluorosilicone rubber	-18.06	-0.16
Delrin acetal resin	-14.91	-0.13
Wood (marine-grade plywood)	-14.05	-0.12
Wear-resistant slippery Garolite	-11.47	-0.10
Super-stretchable and abrasion-resistant natural rubber	-10.61	-0.09
Oil-resistant Buna-N rubber	2.49	0.02
Food-grade oil-resistant Buna-N/vinyl rubber	2.95	0.03

2024

Development of a Flexible Sensor Through Additive Manufacturing for monitoring the progression of Parkinson's Disease

Margarida António